From half-cells to full-cells: across-scale comparative evaluation of lanthanum-based perovskites as high-performance anode materials for the oxygen evolution reaction

Blaž Toplak[§], Leon Müller[§], Ali Raza Khan, André Olean-Oliveira, Khuzaifa Yahuza Muhammad, Wang Feng, Da Xing, Raíssa Ribeiro Lima Machado, Mohammed-Ali Sheikh, Leander Kucklick, Ahammed Suhail Odungat, Philipp Gerschel, Corina Andronescu, Harry Hoster, Christof Schulz, Viktor Čolić, Ulf-Peter Apfel, Hartmut Wiggers, Mohaned Hammad, and Doris Segets**

B. Toplak, A. S. Odungat, Dr. M. Hammad, Prof. D. Segets
Institute for Energy and Materials Processes – Particle Science and Technology, University of Duisburg-Essen, 47057 Duisburg, Germany
E-mail: doris.segets@uni-due.de, mohaned.hammad@uni-due.de

L. Müller, M. A. Sheikh, Prof. C. Schulz, Prof. H. Wiggers
Institute for Energy and Materials Processes – Reactive Fluids, University of Duisburg-Essen, 47057 Duisburg, Germany

R. R. L. Machado, Prof. C. Andronescu
Chemical Technology III, Faculty of Chemistry, University of Duisburg-Essen, 47057 Duisburg, Germany

A. R. Khan, Dr. A. Olean-Oliveira, Dr. V. Čolić
Electrochemistry for Energy Conversion, Max Planck Institute for Chemical Energy Conversion, 45470 Mülheim an der Ruhr, Germany

W. Feng, L. Kucklick, Dr. D. Xing, Prof. H. Hoster
Energy Technology, University of Duisburg-Essen, 47057 Duisburg, Germany

K. Y. Muhammad, Dr. P. Gerschel, Prof. U.-P. Apfel
Activation of Small Molecules – Technical Electrochemistry, Ruhr-Universität Bochum, 44801 Bochum, Germany

Prof. C. Andronescu, Prof. C. Schulz, Prof. H. Hoster, Dr. A. Olean-Oliveira, V. Čolić, Prof. H. Wiggers, Prof. D. Segets
Center for Nanointegration Duisburg-Essen, University of Duisburg-Essen, 47057 Duisburg, Germany

Prof. H. Hoster
The Hydrogen and Fuel Cell Center ZBT GmbH, 47057 Duisburg, Germany

Prof. U.-P. Apfel
Department of Electrosynthesis, Fraunhofer UMSICHT, 46047 Oberhausen, Germany

Keywords: zero-gap full-cell, coherent workflow, spray-flame synthesis, perovskite material, oxygen evolution reaction, alkaline water electrolysis

Abstract

The widespread reliance on evaluating electrocatalysts in electrochemical half-cells presents limitations that hinder a faster transition from academia to industry and can lead to premature exclusion of promising materials. To address these challenges, it is crucial to implement materials testing in application-relevant setups such as zero-gap full-cells. This transition can be achieved through implementing coherent workflows combining rapid evaluation of as-synthesized materials, electrode evaluation at different scales, and post-mortem analysis. This work presents a comparative study of three spray-flame synthesized lanthanum-based perovskite materials ($LaMnO_3$, $LaFeO_3$, and $LaCoO_3$) for the oxygen evolution reaction under alkaline conditions, highlighting different behavior across scales. The research demonstrates how the interplay of materials properties and electrode engineering affects performance under mild and harsh electrochemical conditions. At every step, these perovskites challenge existing literature through unforeseen behavior. Under application-relevant conditions, the results suggest that $LaFeO_3$ (2.09 V) and $LaMnO_3$ (2.16 V), with comparable performance, could potentially replace $LaCoO_3$ (2.07 V). Furthermore, advanced post-mortem techniques provide deeper insight into catalytic activity and structural changes, which cannot be fully explained without preliminary electrochemical half-cell testing. By linking fundamental studies to

application-relevant testing, this research provides knowledge and methods for accelerated material and electrode development.

§ B. Toplak and L. Müller contributed equally to the paper.

1. Introduction

Water electrolysis consists of water decomposition into hydrogen and oxygen through an external energy-driven redox reaction. The oxygen evolution reaction (OER), which occurs at the anode, is kinetically sluggish and represents a major bottleneck in the development of highly efficient anode electrocatalysts. Noble metals, such as Ir and Ru, exhibit adequate OER performance in acidic conditions. However, their scarcity, high cost, and limited stability hinder their practical applications.[1] In contrast, electrolysis in alkaline conditions can be performed with various non-noble metal materials with decent stability. Along this line, perovskite oxide materials (ABO_3, where A represents alkaline-earth or rare-earth metals {Ca, Sr, La} and B represents transition metals {Mn, Fe, Co, and Ni}) have shown promising results in alkaline OER.[2] For instance, La-based perovskites possess the advantage of structural flexibility in the A and B positions, which affects conductivity, stability, and defect formation.[3]

In this study, we focus on three La-based perovskites: $LaMnO_3$, $LaFeO_3$, and $LaCoO_3$ (LMO, LFO, and LCO). The increase of the $Mn^{4+/3+}$ ratio in LMO induces more oxygen bonding with the active Mn^{4+}, leading to improved structural stabilization.[4] LFO combines good redox activity with suitable electronic and ionic conductivity.[5] However, LCO offers superior intrinsic catalytic activity compared to the other two candidates due to the $Co^{3+/4+}$ redox transitions, which promote the formation of oxygen vacancies in the lattice.[3,6] Although several OER studies have investigated previously mentioned perovskites,[7–10] they have typically only been evaluated at laboratory-scale conditions using rotating disc electrodes (RDE) or on nickel foam at low current densities of 10 mA cm^{-2}, with LCO consistently presented as the best pristine perovskite for OER.[7–9,11] In these studies, the perovskite materials were prepared via solution combustion, sol-gel, or co-precipitation synthesis. However, all of these synthesis methods possess distinct drawbacks, including limitations in scalability, cost-efficiency, and control over particle phase, size, shape, and elemental homogeneity, which results in low specific surface areas and hampers catalytic activity.[12] To tackle the aforementioned limitations, this work uses materials based on spray-flame synthesis and presents a direct comparison of La-based perovskite materials. Spray-flame synthesis has proven to be an efficient approach for the production of high-quality phase-pure perovskite nanomaterials with high specific surface and uniform primary particle size (x_p < 10 nm, derived from N_2 adsorption measurements), enabling their use in various applications such as anode materials in OER,[13] water remediation,[14] and selective CO oxidation.[15]

Advancing technology for alkaline water splitting, and in particular for the OER, requires more than just understanding the intrinsic properties of the synthesized materials. It also involves addressing the associated challenges connected to anode preparation, which arise in the case of particle-based, coated catalyst layers from complex interactions between substrate, ionomer, and electrocatalyst. Factors such as ink formulation, ink deposition, substrate selection, and electrocatalyst properties influence adhesion, cohesion, wetting, and overall efficiency.[16,17] This creates a highly complicated system that requires a tailored approach for each electrocatalyst.[13] Another barrier is the slow transition from lab-scale testing in electrochemical half-cells (10-100 mA cm^{-2}, room temperature) toward industry-relevant testing using full-cells ($\geq$ 500 mA cm^{-2}, $\geq$ 50 °C). This hinders the integration of the electrocatalysts into real-life systems early on in the product and process development due to a limited understanding of the material's behavior. To overcome these challenges, we previously developed a highly structured and coherent workflow that enables to evaluate electrocatalyst performance (half- and full-cell testing) in combination with a systematic and trackable material assessment along the process chain, using scalable technologies.[13] This comprehensive approach integrates synthesis, advanced ink formulation, electrochemical testing, and electrode post-mortem analysis, pointing towards pathways for future materials development.

In this research, we emphasize two key aspects critical for further OER advancement. First, we highlight the importance of developing high-quality electrocatalysts and electrode engineering, which may lead to unforeseen performance of OER. Second, we emphasize the need for materials evaluation across scales to gain a comprehensive understanding of the active material's behavior during water electrolysis. By promoting the fast integration of full-cell testing conditions during the material development, we aim to enhance the insights gained from half-cell experiments. Hence, we intensively use electrochemical half-cell testing, as it provides crucial insights into intrinsic material properties that are difficult to obtain from industrial setups. However, we suggest complementing it with the material's exposure to testing conditions that are close to the later application. Bridging this gap can help avoid unjustified or premature elimination of promising materials after initial lab-scale testing. Additionally, incorporating post-mortem analysis strengthens the understanding of the mechanistic behavior of perovskites under harsh electrolyzer conditions, which will pave the way for the efficient design and engineering of next-generation electrocatalysts.

2. Results and discussion

2.1. Catalytic nanopowder characterization

All three perovskite materials were synthesized using spray-flame synthesis with identical solvents and concentration ratios of the respective precursors. Their structures and compositions were analyzed using X-ray diffraction (XRD, **Figure 1**a) and Raman spectroscopy (Figure 1b). LMO and LFO diffraction peaks can be indexed to the single-phase orthorhombic structure matching ICSD 51653 and ICSD 7794, respectively.[18] Conversely, the diffraction pattern of LCO matches the rhombohedral perovskite $LaCoO_{2.925}$ structure (ICSD 153993).[10] The phase compositions of the perovskite materials were additionally assessed with Raman spectroscopy at room temperature, which has the advantage of being more sensitive to oxygen motion and structure distortion.[19] The Raman spectra of LMO reveal two strong vibrational modes at around 495 and 622 cm^{-1}, which are attributed to the Jahn-Teller distortion of MnO_6 octahedra.[20,21] Likewise, in the LFO, Raman modes at 435 cm^{-1} are related to oxygen bending vibrations, while stretching Raman modes of FeO_6 octahedra are observed at 636 cm^{-1}. These findings for both materials are consistent with the orthorhombic structural configuration previously determined through XRD.[22–24] Furthermore, the Raman mode in LCO at 640 cm^{-1} corresponds to Co–O stretching vibrations, providing additional support for the rhombohedral arrangement of LCO.[25,26]

To investigate the surface properties and valence states of all three perovskite powders, X-ray photoelectron spectroscopy (XPS) analysis was performed. In all cases, lanthanum (Figure S1a, Supporting Information) is present as La^{3+}. The $La3d_{5/2}$ multiplet splitting shows energy differences of 3.7, 3.7, and 3.8 eV for LMO, LFO, and LCO, respectively. These values are consistent with those reported in the literature for lanthanum-based perovskites.[27,28] The surface spectra of $Mn2p_{3/2}$ (Figure S1b, Supporting Information) deconvoluted by peaks at 641.1 and 642.8 eV, belong to Mn^{3+} and Mn^{4+} species, where manganese is predominantly in the Mn^{3+} valence state.[29] The two $Fe2p_{3/2}$ peaks (Figure S1c, Supporting Information) positioned around 710.2 and 711.9 eV indicate the presence of a mixed oxidation state of Fe^{2+} and Fe^{3+}, respectively.[30] The $Co2p_{3/2}$ (Figure S1d, Supporting Information) spectra are also fitted with two individual peaks at 779.7 and 781.4 eV, corresponding to the Co^{3+} and Co^{2+} oxidation states.[31,32] The main O1s XPS spectra for all materials were deconvoluted into two components (Figure S1e, Supporting Information) at around 528.8 and 531.5 eV, respectively,

indicating predominantly lattice oxygen ($O_{lattice}$) and adsorbed hydroxyl species ($O_{surface}$) on the surface.[32]

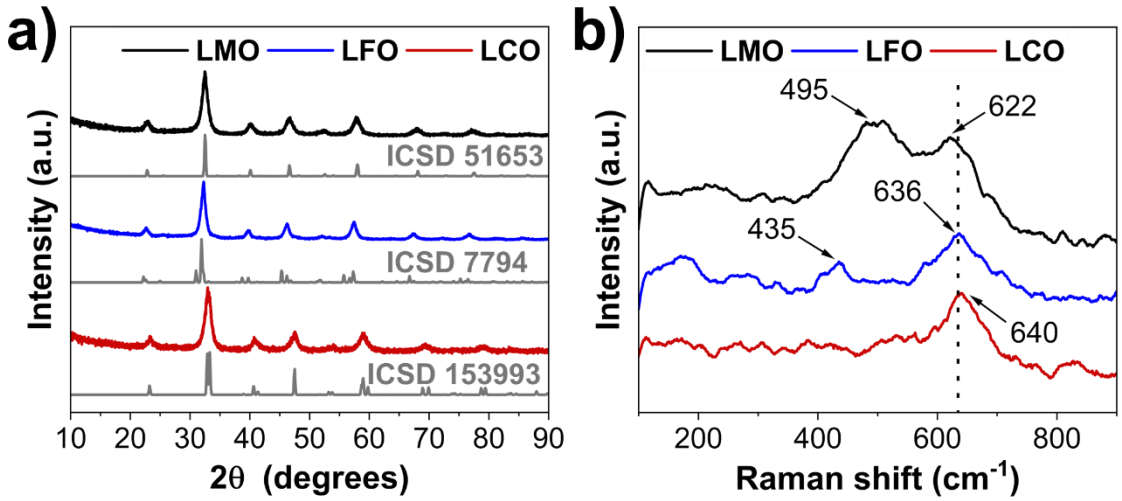

Figure 1. (a) XRD patterns of spray-flame synthesized LMO (black), LFO (blue), and LCO (red), with corresponding ICSD references 51653, 7794, and 153993 (grey). (b) Raman spectra of LMO (black), LFO (blue), and LCO (red).

The morphological and elemental analysis of spray-flame synthesized perovskite materials was performed using transmission electron microscopy (TEM) and energy dispersive X-ray mapping (EDX) (Figure 2a–c, Figure S2a–c, Supporting Information). All three materials are confirmed to be mainly present as quasi-spherical primary nanoparticles with distinct edges, while the EDX analysis evidences a uniform elemental distribution in all three perovskites. Furthermore, high-resolution TEM (HRTEM) images of LMO and LFO (Figure 2d–e) show interplanar spacing of 0.281 nm for LMO, corresponding to the (011) orthorhombic lattice plane, and 0.285 and 0.395 nm for LFO, matching the (121) and (101) lattice planes, respectively.[14] Moreover, the HRTEM image of LCO (Figure 2f) exhibits crystal lattice fringes with an interlayer spacing of 0.273 nm, corresponding to (104) rhombohedral planes, consistent with the XRD and Raman spectroscopy analysis.[33] Additionally, the specific surface area was examined using the Brunauer-Emmett-Teller (BET) method. The measured specific surface of LMO, LFO, and LCO were 105.2, 94.2, and 84.6 $m^2 g^{-1}$, with corresponding calculated primary particle sizes (d_p^{BET}) of 8.7, 9.6, and 10.0 nm, respectively.

In total, combining all structural and surface characterizations confirmed that all three nanopowders possess phase-pure perovskite structures with high surface area, which is crucial for enhancing the accessibility of active sites.

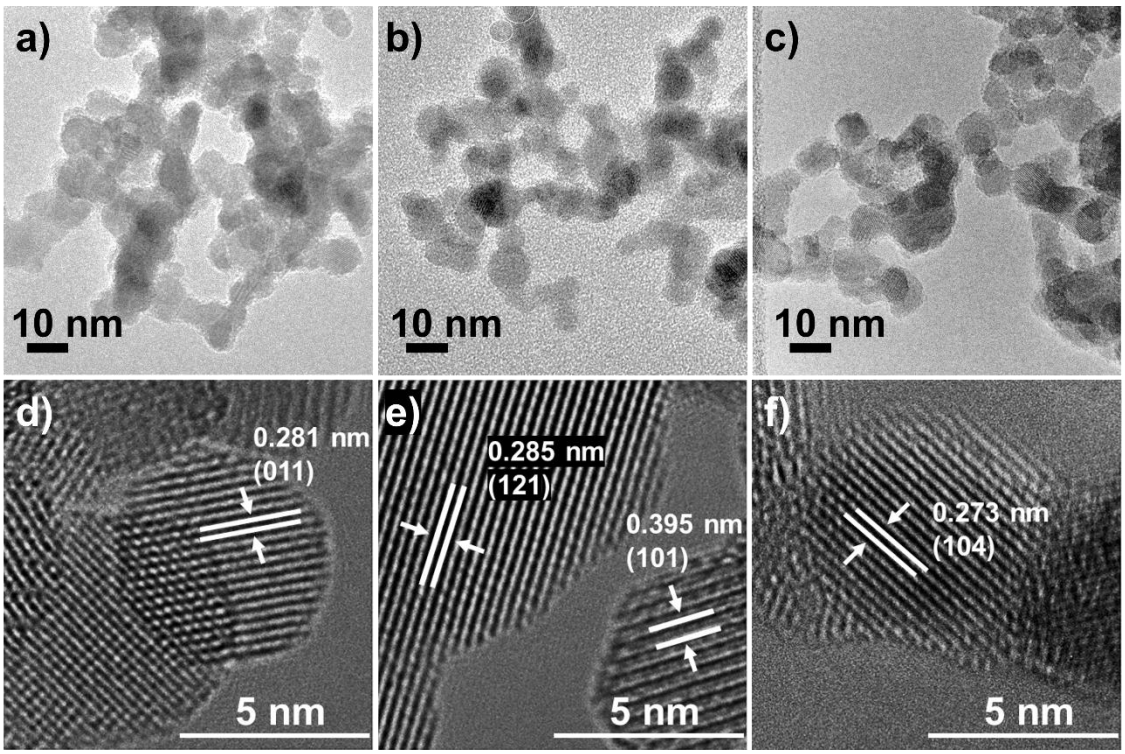

Figure 2. TEM images of LMO, LFO, and LCO nanopowders (a, b, and c). HRTEM images of LMO, LFO, and LCO perovskite materials (d, e, and f).

2.2. Powder wetting, dispersion, and ink characterization

Understanding interactions between nanoparticles, additives, and solvents is important for efficient electrode fabrication and the successful transition from lab-scale to larger-scale processes. The key to a smooth transition is the preparation of homogeneous and stable dispersions from non-toxic, environmentally and economically feasible solvents and additives/binders. To investigate interactions of LMO, LFO, and LCO nanoparticles with different solvents or probe liquids (PLs), the method of HSP (Hansen solubility parameters, where in the case of powders the 'S' should be rather understood as similarity) was utilized, which was adopted by us to assess particulates.[34,35] Thereby, the selection of PLs plays a crucial role in determining the surface properties of perovskite nanoparticles. For that reason, a two-step method developed by Amin et al.[36] was introduced. LMO, LFO, and LCO were initially dispersed in polar protic, polar aprotic, and moderate polar PLs, including ethanol, dimethylformamide, tetrahydrofuran, 2-propanol, dimethylsulfoxide, and acetone. The interactions and stability of perovskite nanoparticles in the PLs were visualized using transmittograms (Figure S3–S5, Supporting Information), which provide the qualitative and quantitative characteristics of the physical properties of complex colloidal or dispersed

systems.[37] For the calculation of the HSP sphere, the interaction of perovskites with different PLs were finally categorized on the basis of relative sedimentation times of the settling dispersion during analytical centrifugation. Using the HSPiP software and the automated addition method developed by Süß et al. and Anwar et al., the ordering of PLs into good and poor was done (Figure S6, Supporting Information).[38,39] Transmittograms reveal similar interactions in LMO and LFO, resulting in the same PL ranking and HSP. Both materials demonstrate good dispersibility in polar protic ethanol and 2-propanol, as well as polar aprotic dimethylformamide. In contrast, moderate polar PLs tetrahydrofuran, acetone, and polar aprotic dimethylsulfoxide, are classified as poor. LCO shows good dispersion stability in polar protic ethanol and polar aprotic dimethylformamide and dimethylsulfoxide, while 2-propanol, tetrahydrofuran, and acetone were classified as poor. Differences in HSP are explained by distinct crystal structures, which affect the interactions between the nanoparticle surface and the probe liquid molecules.[34,40] These differences are reflected in the elevated δ_D and δ_P values of LCO compared to LMO and LFO, resulting in a larger radius of the Hansen sphere (Figure S6, Table S1, Supporting Information).

For further understanding of the interaction between perovskites and PLs, Fourier-transform infrared spectroscopy (FTIR) measurements (Figure S7, Supporting Information) of powders were performed. Vibration modes at 850 cm^{-1} in all three materials are associated with Mn−O, Fe−O, and Co−O vibrations.[41] The presence of vibration modes between 1300 and 1600 cm^{-1} indicates the presence of organic residues on the surface after spray-flame synthesis. The vibrations in LMO and LFO samples at 1372 and 1479 cm^{-1} are related to the C−H vibration modes,[42,43] while additional vibrations noticed just in LMO at 1420 and 1578 cm^{-1} are attributed to C−H and C=C bonds.[44] Vibrational modes in LCO appear at 1315, 1420, and 1530 cm^{-1}, corresponding to O−C=O, O−H, and C=C vibrations.[42,43] Above 3000 cm^{-1}, it is noted that LMO and LFO possess a significantly higher amount of surface O−H groups than the LCO particles, which correlates perfectly with the HSP data.[42]

Based on the HSP, ethanol was found as a suitable continuous phase for dispersing the three perovskites and was selected as the solvent for the subsequent ink formulation. However, ethanol is a common solvent used in various applications and technological processes, resulting in a massive demand, which has led to increased prices over the last few years.[45,46] Lowering production costs can be achieved by introducing water into the system.[46,47] In contrast to inks solely based on ethanol, the use of water/alcohol mixtures has been observed to impede crack formation and the occurrence of film delamination during drying, mainly stemming from the rapid evaporation of ethanol at elevated temperatures.[48] Therefore, stability characterization

of the catalysts in ethanol, water, and various mixtures of water/ethanol (50/50, 75/25, and 90/10 v/v%) was conducted (Figure S8–S10, Supporting Information). Results for all three perovskites show a similar trend of reducing the stability of dispersions and faster material sedimentation with the increasing concentration of water. According to the results on dispersion stability, a water/ethanol mixture of 75/25 v/v% is selected as the continuous phase for further formulations, as it presents a good compromise between costs and stability (Figure 3a–c).

Upon selecting the suitable solvent, inks were formulated by the incorporation of Sustainion® as a binder. Our previous findings indicate that incorporating fluorine-free Sustainion® in the electrode preparation of $La_{0.8}Sr_{0.2}CoO_3$ and $NiFe_2O_4$ nanomaterials significantly improved electrode durability, enhancing their performance in the OER.[13] As demonstrated in all cases (Figure 3d–f), the addition of Sustainion® in small concentrations improved the ink stability, resulting in decreased sedimentation over time.

Altogether, we believe that this structured process for ink development and improvement will play an important role in scale-up reproducible electrode fabrication.

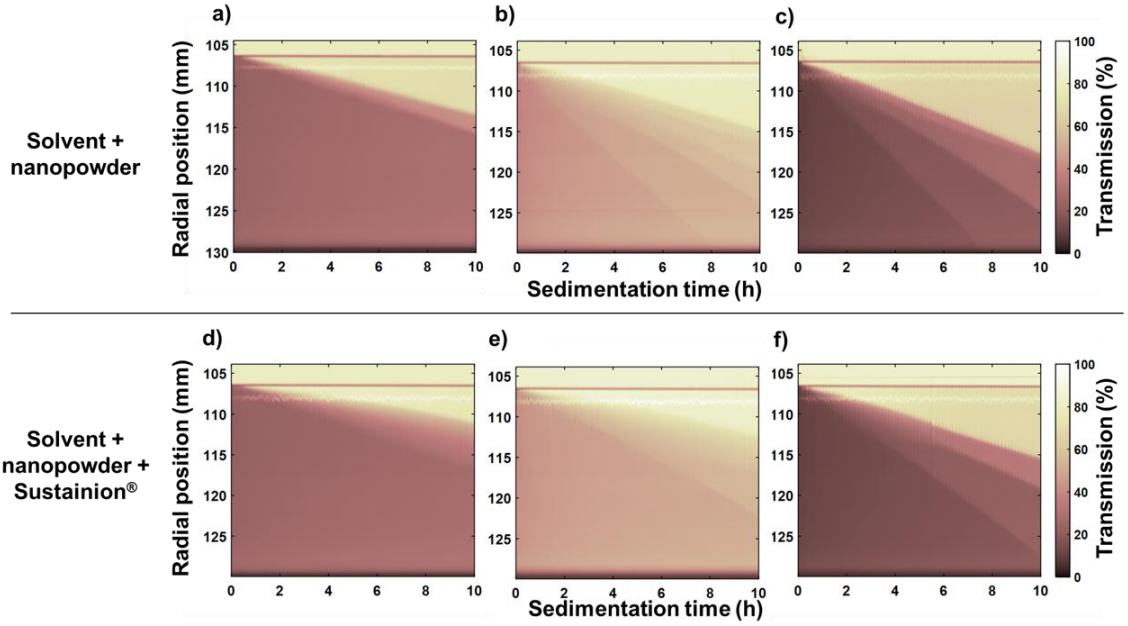

Figure 3. Transmittograms of LMO, LFO, and LCO dispersions in H2O/EtOH 75/25 v/v% (a, b, and c). Transmittograms of LMO, LFO, and LCO inks with Sustainion® binder in H_2O/EtOH 75/25 v/v% (d, e, and f). Darker colors present low transmission and better phase stability over time.

2.3. Structural characterization of catalyst-coated nickel-substrate anode electrodes

The surface morphology and roughness of the LMO-, LFO-, and LCO-based thin-film electrodes were assessed using a scanning electron microscope (SEM), EDX, and atomic force microscopy (AFM). The SEM measurements (Figure 4a–c) confirm that all three electrodes exhibit smooth and slightly porous structures, while EDX analysis indicates uniform elemental distribution across all electrodes. This includes the organic component from the Sustainion® binder (Figure S11–S13, Supporting Information), indicating good dispersibility in a water/ethanol environment. Furthermore, AFM (Figure 4d–f) was employed to analyze surface characteristics represented by the square mean root roughness (*S*q) values. The *S*q values assessed for LMO-, LFO-, and LCO-based electrodes are situated between 155 – 180, 160 – 200, and 180 – 220 nm, respectively. The slight rise in surface roughness can be attributed to the increased perovskite nanoparticle size from LMO towards LCO, as confirmed by TEM and BET analysis. The increase in particle size can also explain the increase in pore surface coverage and average pore size distribution from LMO towards LCO (Figure S14–S15, Supporting Information, **Table 1**). It is worth noting that surface roughness and porosity affect the presence of active sites, mass transport, and catalytic performance.[17,49–51] Therefore, additional contact angle measurements were performed (Figure S16a, Supporting Information), where no significant differences were observed, underpinning constant wetting properties across all three anode materials.

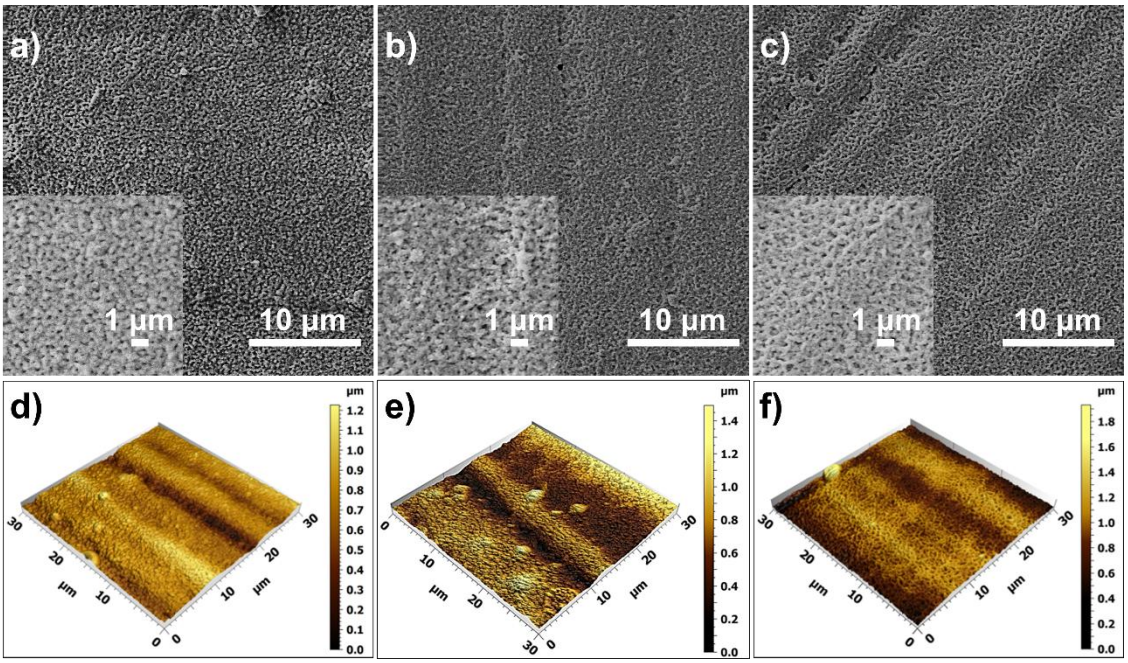

Figure 4. SEM images of electrodes made by spray-coating of Sustainion®-containing LMO-, LFO-, and LCO-based inks on nickel substrates (a-c). AFM topography images of LMO-, LFO-, and LCO-based electrodes (d-f).

To summarize, Table 1 presents the most important parameters for OER. Taking into account the powder synthesis and electrode engineering of our catalysts (including ink formulation, electrode fabrication, and surface characterization), we can conclude that our methodology enables fast, reproducible, and scalable electrode manufacturing. The synthesized powders exhibit similar properties, with a slightly higher surface roughness and porosity of the LCO-based electrodes. As expected, the combination of comparable synthesis conditions and electrode engineering enables the generation of anodes for which the OER performance will be primarily connected to intrinsic properties of the active material rather than to the structure-driven electrolyte wettability.

The prepared electrodes will be electrochemically evaluated in the next sections using different electrochemical techniques to investigate how the combination of intrinsic material and electrode properties affects the OER performance.

Table 1. Powder and electrode parameters relevant for the OER performance

Nanopowder parameters			
x_p^{BET} / nm	8.7	9.6	10.0
BET / $m^2\ g^{-1}$	105.2	94.2	84.6
XPS / [$O_{surface}$ /$O_{lattice}$]	0.83	0.94	0.90
HSP			
$\delta_D/\delta_P/\delta_H/R$ / $Mpa^{0.5}$	16.5/10.7/15.0/5.1	16.5/10.7/15.0/5.1	17.1/12.6/14.9/6.6
Electrode parameters			
*S*q roughness / nm	155 – 180	160 - 200	180 – 220
Surface pore coverage / %	8.6	8.8	10.6
Contact angle / °	85	89	91

2.4. Electrochemical characterization of catalyst-coated electrodes

2.4.1. Scanning droplet cell tests

The lateral homogeneity of the 1 × 1 cm^2 nickel (Ni)-plates coated with 250 µg cm^{-2} LMO, LFO, and LCO with Sustainion® as a binder was assessed by scanning droplet cell (SDC, analysis (Figure S17, Supporting Information). For each coated electrode, the electrocatalytic activity was evaluated based on 25 measured areas that were analyzed and spaced 1.8 mm apart (Figure S18, Supporting Information, spot area of 0.0021 ± 0.0002 cm^2). Figure S19 (Supporting Information) presents the average and standard deviation of the LSVs. LFO-based electrodes exhibit the lowest overpotential value (η) for OER at 10 mA cm^{-2} (1.541 ± 0.002 V vs. RHE) of the investigated catalyst-coated electrodes. At the same current density, the LCO-based electrodes follow with an inferior activity (1.560 ± 0.003 V vs. RHE), while the lowest activity among the coated electrodes is observed for the LMO-based electrodes (1.635 ± 0.007 V vs. RHE). The differences in overpotential among the electrodes were statistically significant ($p < 0.05$).

The homogeneity of the coatings for OER activity is also represented in the activity maps (Figure S20a–b, Supporting Information). The current densities of the 25 individual measured areas of each coated electrode and their relative standard deviation compared to the average of the sample across the spots are represented at a potential of 1.541 V vs. RHE. LFO-based electrodes (8.8 mA cm^{-2}) exhibited a superior average current density compared to LCO-based

electrodes (7.4 mA cm^{-2}) and lastly to the LMO-based electrodes (4.9 mA cm^{-2}). The homogeneity of the OER activity is also evident in the standard deviations of ±16.4, ±11.6, and ±7.6 % of LMO-, LFO-, and LCO-based electrodes, along with their respective maximum deviations of 42.1, 25.6, and 16.3 %, respectively. Despite the coated films appearing visually homogeneous before the SDC measurements (Figure S21, Supporting Information), the LMO-based electrode surface was more damaged after measurements due to the additional force needed to seal the SDC and prevent electrolyte leakage. This result aligns with previous reports indicating that LMO exhibits less efficient activity compared to LCO and $LaMn_xCo_yO_3$-based perovskites.[52]

In brief, the homogeneity of electrochemical activity for OER was successfully investigated using high-throughput SDC. This automated, versatile, and efficient technique enables precise screening of electrode surfaces, thus providing preliminary data to support and accelerate the development and scaling up of new electrocatalysts. However, at this point, the superior performance of the LFO-based electrodes compared to LCO- and LMO-based electrodes raises additional questions, which are discussed in the next section.

2.4.2. Rotating disc electrode, compression cell, and flow cell coupled with inductively coupled plasma-optical emission spectrometry (ICP-OES) experiments

In the scaling-up process, accurately determining the electrocatalytic activity is essential for identifying promising candidates and discarding materials with insufficient performance. Electrochemical evaluation typically includes RDE measurements (Figure S22, Supporting Information), with glassy carbon (GC) being the most commonly used support material. This is often followed by tests on three-dimensional (3D) metal-based supports, such as Ni foam.[13] As highlighted in our previous study, an important consideration is the potential impact of support-catalyst interactions on the catalyst's performance, which could affect its activity.[53] To investigate this further, we performed electrochemical measurements in the RDE system using both GC and Ni as support materials, where the induced rotation reduced mass transport limitations and facilitated oxygen bubble removal.[54] Figure 5a-b presents the activity of LFO, LCO, and LMO deposited on a GC and Ni electrode support in a conventional RDE system. The observed trends were similar for both systems, except for the LMO-based electrode, which showed no electrocatalytic activity when GC was used as the support material. In general, the potential values recorded at 10 mA cm^{-2} presented higher overpotentials when the GC was employed as the support.

Subsequently, electrochemical impedance spectroscopy (EIS) measurements were conducted at a potential of 1.6 V vs. RHE to gain further insight into the electrochemical behavior, as shown in Figure S23a–c (Supporting Information). The Nyquist plot revealed significant differences in the charge transfer resistance (R_{ct}) based on the capacitive arc diameter. For instance, the LFO-based electrode exhibited an $R_{ct} \approx 6\ \Omega$ for Ni-coated electrodes and 235 Ω for GC-coated electrodes. The higher value of R_{ct} observed for GC can be attributed to the potential dissolution/deactivation of LMO and inactivity towards OER.

Notably, for the LCO-based electrode, two distinct capacitive arcs were observed, indicating two processes with different time constants at the catalyst layer/electrode interface, due to differences in capacitive and resistive properties when Ni is used as the support electrode.[55] This second time constant is evident in the Bode plot (Figure S24a–b, Supporting Information), which shows two peaks at approximately 3000 and 10 Hz. The additional interface may affect the electrocatalytic activity by introducing electron transfer from the catalyst to the electrode or by charging the interface through accumulating charge. In contrast, the LFO- and LMO-based electrodes exhibit a single time constant. Further investigation will be carried out in a dedicated study for a better understanding.

Additional support for the improved intrinsic properties of the LFO-based electrode in relation to the OER performance can arise from prior density theory calculations. Tripkovic et al.[56] correlated higher overpotential of LCO to changes related to the valence state of the metal center and differences in the number of hydroxyl species on the surface. This is experimentally validated with our XPS results, where the LFO shows the highest hydroxyl group surface coverage ratio (Table 1).

The compression cell (Figure S25, Supporting Information)[57] enables the exposure of the electrode surface area to the electrolyte under uniform potential distribution across the exposed area. During the measurements, the oxygen is not removed and remains in close vicinity of the electrode.[13] LSV measurements (Figure S26, Supporting Information) of electrocatalysts at 10 mA cm^{-2} revealed that the LFO-based electrodes demonstrated the best performance, achieving 1.54 V vs. RHE, closely followed by the LCO-based electrodes with 1.57 V vs. RHE, aligning well with the SDC results. In contrast, the LMO-based catalyst performed significantly worse, with a value of 1.73 V vs. RHE, compared to the other two materials. This is partially attributed to the electrochemical surface area (ECSA, Figure S27a–d, Table S2–S3, Supporting Information), which is significantly lower compared to LFO- and LCO-based electrodes (0.30, 0.57, and 0.55 cm^2). After approximately 41 mA cm^{-2}, a crossover point in the LSV-curves of the LFO- and LCO-based electrodes is observed. This could be attributed to two possible

scenarios. The first is related to the configuration of the electrochemical cell, and the second is the activation of the LCO-based electrodes connected to material segregation.[58] These hypotheses will be evaluated in the following through post-mortem analysis following long-term stability testing. Subsequent chronopotentiometric stability (CP) measurements (Figure 5c) were performed at 10 mA cm^{-2} for 12 h. The same trend was noted from the LSV across the whole measurement window. During the measurement period, LFO-, LCO-, and LMO-based electrodes showed a slight increase from their initial potential to 1.56, 1.59, and 1.85 V vs. RHE, respectively. Furthermore, low standard deviations of LFO- and LCO-based electrodes suggest good reproducibility of these electrodes under laboratory conditions.

Following the compression cell measurements, post-mortem morphological and elemental evaluations were conducted using EDX, SEM, and AFM. The EDX analysis (Figure S28–S30, Supporting Information) exhibits uniform elemental distribution. SEM images (Figure S31a–c, Supporting Information) reveal that all electrodes maintain a homogeneous coating after their exposure to the electrochemical treatment, with some randomly allocated agglomerates. However, in the case of LCO-based electrodes, surface cracks are observed post-electrochemical testing. The AFM analysis (Figure S31d-f, Supporting Information), conducted after stability testing for 12 h, shows a reduction in the *S*q values, while the trend amongst different materials remains as observed in the case of the pristine electrodes. Among the electrocatalysts, LMO-based electrodes exhibit the smoothest surface with minimal variations across the area. The *S*q values range between 85 – 95 nm, followed by LFO-based electrodes, with *S*q values between 110 –130 nm. The LCO-based electrodes display the highest *S*q values, ranging from 140 – 180 nm, respectively. Similarly to the SEM, AFM also revealed cracks on the surface of LCO-based electrodes, which indicates and supports the hypothesis on material-segregation that was deduced from the crossing of the LSV-curves in Figure S26 (Supporting Information). Moreover, grazing-incidence X-ray diffraction (GIXRD) was employed to investigate the potential changes in the crystal phase after compression cell measurements (12 h at 10 mA cm^{-2}). While GIXRD (Figure S32a–c) did not reveal any significant phase changes in LMO-, LFO-, and LCO-based electrodes after electrochemical stress, the strong diffraction signals from the nickel substrate likely masked subtle structural modifications in the perovskite phases, potentially limiting the detection of minor phase transformations.

Overall, structural characterization under laboratory conditions did not reveal significant changes in the electrode surface morphology and composition. This good structural stability is crucial before subjecting the materials to harsher conditions, as unstable materials should not be considered for further testing at application-conditions.[13]

Integrating the electrochemical cell with ICP-OES (Figure S33, Supporting Information) enables the direct analysis of reaction products and establishes a link between dissolution behavior and the electrochemical operation.[59] The configuration plays a vital role in regulating transport processes, including diffusion, convection, and migration of reactive products and bubbles away from the electrode. Additionally, it introduces mechanical stress on the electrode surface, facilitating the investigation of the electrochemical stability.[60]

During these measurements, a minor transient of Fe and Mn dissolution (Figure S34a, Supporting Information) is observed, independent of the applied potential. The leaching behavior of the metal ions is summarized in Figure S26b (Supporting Information). During OER operation, Fe and Mn dissolution is detectable at a current density of 5 and 10 mA cm^{-2}, resulting in approximately 0.25 ng s^{-1} cm^{-2} for Fe and 0.68 ng s^{-1} cm^{-2} for Mn. The dissolution rate of Fe increases transiently and slowly decreases until the end of the hold. The calculated dissolution should be treated with caution under these operating conditions, as it is below the nominal detection limit of the online ICP-OES system. However, manganese leaching may be a partial reason for the poor electrochemical performance of LMO-based electrodes, as discussed previously during RDE measurements. Furthermore, no La or Co dissolutions are observed during OER operation at steady-state current.

In conclusion, the OER performance of perovskite catalysts was systematically evaluated using three different complementary lab-scale electrochemical techniques, providing in-depth insights into their performance at low current densities. The findings are in good agreement with the previously used SDC technique. Our results are in sharp contrast with the previously mentioned studies from the literature that identified LCO powder as the most effective electrocatalyst. However, perovskites in those studies were obtained from different synthesis techniques.[7–9] This deviation suggests that the superior performance of the LFO-based electrode may be attributed first, to the distinctive intrinsic properties of the spray-flame synthesized material that provides only minute amounts of organic residuals at the surface, and second, advanced electrode engineering that enables comparable anodes with only slight variations in the electrode microstructure, which have not been reported before. Although the LMO-based electrodes exhibited substantially higher overpotential, making it less promising, it will still be examined further under application-relevant conditions for a more comprehensive assessment of its capabilities.

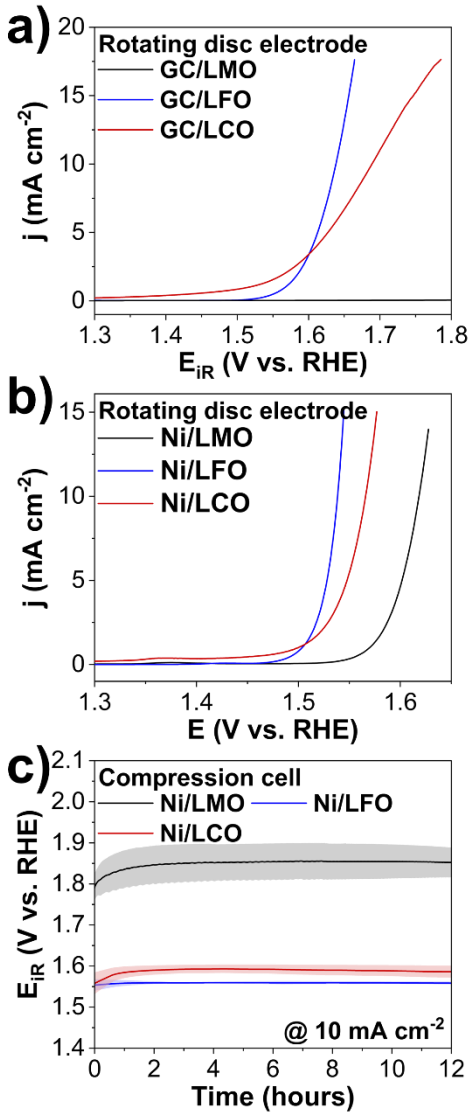

Figure 5. LSV curves of LMO- (black), LFO- (blue), and LCO-based electrodes (red) with Sustainion® obtained with the RDE (1600 rpm, O_2-saturated, purified 1 mol L^{-1} KOH) on glassy-carbon and nickel substrate (a, b). The shift to lower overpotentials is connected to material conductivity. CP measurements were recorded with the compression cell in a purified, O_2-saturated, 1 mol L^{-1} KOH. The solid lines correspond to the mean values, and the shadows represent their standard deviations (c).

2.4.3. Zero-gap full-cell test

Next, anode-testing based on the coherent workflow transitions to the scalable zero-gap full-cell setup (Figure S35, Supporting Information) with membrane electrode assembly (MEA), making a significant step toward industrial applicability. In our previous study, we highlighted that polarization curves (equivalent to the LSV curves in the half-cell) and long-term stabilities

at high current densities are key indicators of whether the combination of catalytic material, binder, and substrate is suitable for future development toward real-life applications.[13] Two trends are noticed in the polarization curves. The first one at 0.5 A cm^{-2} indicates that the polarization curves (Table 2, Figure S36a–d, Supporting Information) mainly follow the trend noticed with the electrochemical standard laboratory half-cell electrochemical setups. The most significant difference is detected in polarization curves obtained after 36 h of electrochemical testing, where the LCO-based electrodes, for the first time, outperform LFO-based electrodes (Figure S36d, Supporting Information). Second, the polarization curves of the LMO-based electrodes are much closer to the LCO- and LFO-based electrodes, indicating that the LMO-based anodes under application-relevant conditions show enhanced performance compared to the results gained at 10 mA cm^{-2}. Long-term stability CP measurements (Figure 6) were obtained at a current density of 0.5 A cm^{-2} for 12 h at room temperature and additionally for 24 h at 60 °C. After exposure for 12 h at room temperature, the cell potential (U_{cell}) of LMO- (2.32 V) and LCO-based electrodes (2.20 V) is relatively stable. In contrast, in the case of LFO-based electrodes (2.17 V), a significant increase in the potential is recorded. This further confirms that the overpotential of LMO-based electrodes during application-relevant conditions is significantly closer to the other two electrocatalysts than suggested by electrochemical half-cell testing.

Furthermore, to simulate real-life electrolyzer conditions more accurately, additional full-cell tests were conducted at 60 °C. In all cases, the elevated temperature led to a significant improvement in U_{cell}. The most substantial decrease in U_{cell} is observed with LMO-based electrodes (0.28 V) compared to the U_{cell} after testing at room temperature, followed by LFO- and LCO-based electrodes with 0.24 and 0.22 V, respectively. Similarly to room temperature measurements, the LFO-based electrodes again show the highest increase of the U_{cell} with time (0.15 V), followed by LMO- (0.12 V) and LCO-based electrodes (0.09 V), aligning with the trends observed in the polarization curves. After 36 h exposure, the LCO-based electrodes show lower U_{cell} compared to LFO- and LMO-based electrodes (2.07, 2.09, and 2.16 V).

This leads to a couple of conclusions. Firstly, all three perovskite electrocatalysts show promising performance for OER under application-relevant conditions. This includes the LMO-based electrodes, which would typically be discarded after the lab-testing conditions. Secondly, after 36 h, all electrocatalysts reach a plateau, indicating a steady state of the system. Thirdly, the curve-crossing trends observed between LFO- and LCO-based electrodes point towards material changes that are only evident under harsh conditions and are unknown

to standard laboratory electrochemical testing. These changes will be investigated in the post-mortem analysis section.

Table 2. Electrochemical results on the three perovskites gained by electrochemical half-cell-testing at 10 mA cm^{-2} in purified, O_2-saturated, 1 mol L^{-1} KOH and results gained under application-relevant conditions with the zero-gap full-cell at 0.5 A cm^{-2} in as-prepared 1 mol L^{-1} KOH at room temperature and 60 °C.

	LMO / V vs. RHE	LFO / V vs. RHE	LCO / V vs. RHE
SDC / 10 mA cm^{-2}	1.635 ± 0.007	1.541 ± 0.002	1.560 ± 0.003
RDE/GC / 10 mA cm^{-2}	/	1.64	1.69
RDE/Ni / 10 mA cm^{-2}	1.62	1.54	1.57
Compression cell / 10 mA cm^{-2}	1.731 ± 0.007	1.54 ± 0.01	1.566 ± 0.004
	voltage / V	voltage / V	voltage / V
Zero-gap full-cell before CP at room temperature / 0.5 A cm^{-2}	2.27 ± 0.05	1.96 ± 0.09	2.14 ± 0.01
Zero-gap full-cell after CP at room temperature / 0.5 A cm^{-2}	2.23 ± 0.04	2.04 ± 0.03	2.15 ± 0.02
Zero-gap full-cell before CP at 60 °C / 0.5 A cm^{-2}	2.00 ± 0.03	1.86 ± 0.02	1.94 ± 0.05
Zero-gap full-cell after CP at 60 °C / 0.5 A cm^{-2}	2.08 ± 0.05	2.018 ± 0.002	1.97 ± 0.05

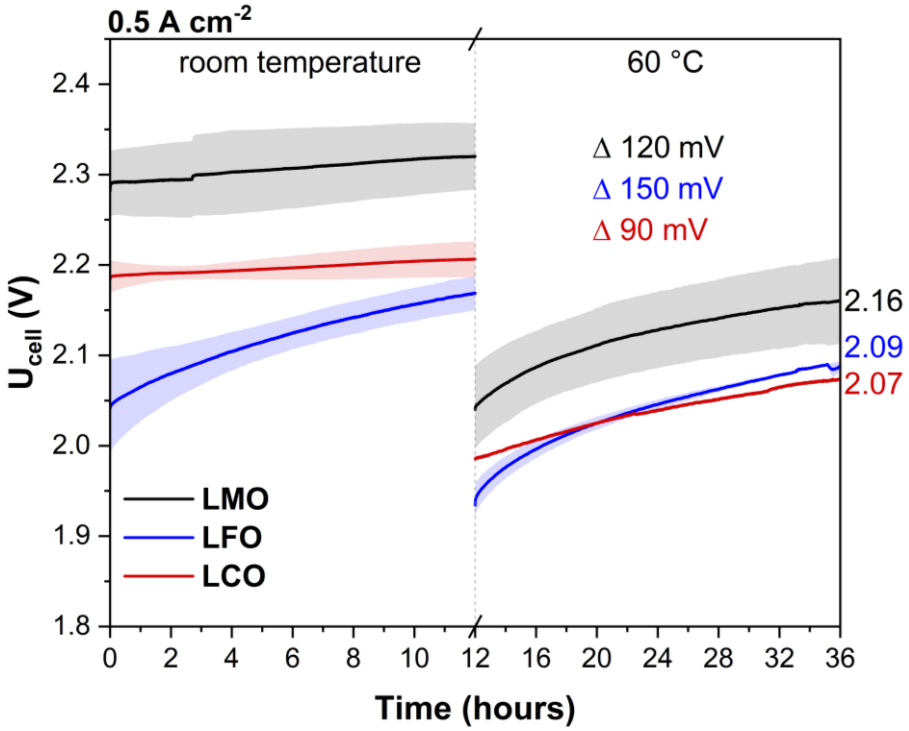

Figure 6. Zero-gap full-cell characterization of LMO- (black), LFO- (blue), and LCO-based electrodes (red) at room temperature and 60 °C at 0.5 A cm^{-2} in as-prepared 1 mol L^{-1} KOH on Ni foam substrates.

2.5. Post-mortem full-cell analysis

To gain a deeper understanding of performance changes, post-mortem analysis of the anodes after full-cell testing at room temperature and 60 °C was conducted using Raman spectroscopy, XPS, and GIXRD. These results were compared to pristine electrodes (Pristine) that were not exposed to electrochemical conditions. This enables us to understand catalytic mechanisms and provides, together with the electrochemical data, a comprehensive understanding of the materials' behavior under real-life operating conditions.

2.5.1. Post-mortem analysis of the thin films by Raman spectroscopy

Raman spectroscopy of all the LMO-based electrodes (Figure 7a–c) reveals two vibrational modes at 498 and 616 cm^{-1}, corresponding to Jahn-Teller distortion in the MnO_6 octahedra.[20,21] The full-cell testing at room temperature of the LMO-based electrode exhibits no significant differences from the pristine-LMO-based electrode before electrochemical testing. However, an additional Raman mode at 572 cm^{-1} is observed after full-cell testing at 60 °C. This is

attributed to the Mn−O stretching vibration, indicating an increased presence of Mn^{4+}.[61] For LFO-based electrodes, a Raman mode at 642 cm^{-1} is detected in both the pristine-LFO-based electrode and LFO-based electrode after full-cell testing, corresponding to the FeO_6 octahedral stretching vibrations.[22,24] However, after full-cell testing at 60 °C, new Raman modes appear at 572 and 666 cm^{-1}, indicating an increased presence of Fe^{3+} due to surface changes most likely caused by chemical leaching under harsh conditions.[62] The leaching and deposition of iron on the surface align well with the ICP-OES data described above (electrochemical flow cell coupled with ICP-OES), where traces of iron were detected. On the other hand, lanthanum showed no dissolution.

These changes were additionally confirmed by EDX mapping of the LFO-based electrode after full-cell testing at 60 °C (Figure S37, Table S4, Supporting Information), which revealed localized areas of increased iron concentration. In the case of LCO-based electrodes, the pristine-LCO-based electrode exhibits a Raman mode at 642 cm^{-1}, corresponding to the Co−O stretching vibrations.[25,26] After electrochemical exposure at 0.5 A cm^{-2}, a significant shift of 49 cm^{-1} is observed. The peak at 593 cm^{-1} in the LCO-based electrode after full-cell testing at room temperature and 60 °C is associated with the Co−O vibrations and formation of amorphous $CoO_x(OH)_y$. Additionally, the exposed shoulder is related to the Co−O−Co vibrations.[63] Moreover, TEM (Figure S38, Supporting Information) was used to confirm the formation of an amorphous structure with a coexistence of crystalline and amorphous phases. The amorphization and catalytic mechanism were further validated using CV taken from the compression cell (Figure S39, Supporting Information).[64,65] Notable changes between the 1st and 10th or 50th cycle suggest that the LCO-based electrode underwent irreversible conversion from Co(II) to Co(III), which can be related to the formation of $CoO_x(OH)_y$ on the surface.[58,66] This is in line with findings from Li et al.[67] who demonstrated that the amorphization process of LCO improves the activity of the electrocatalyst, which may explain the significantly improved stability of LCO-based electrodes at 0.5 A cm^{-2} in comparison to LFO- and LMO-based electrodes. Similar studies by Cai et al.[68] and Indra et al.[69] also support the observation that amorphous catalysts exhibit superior activity and stability compared to crystalline structures.

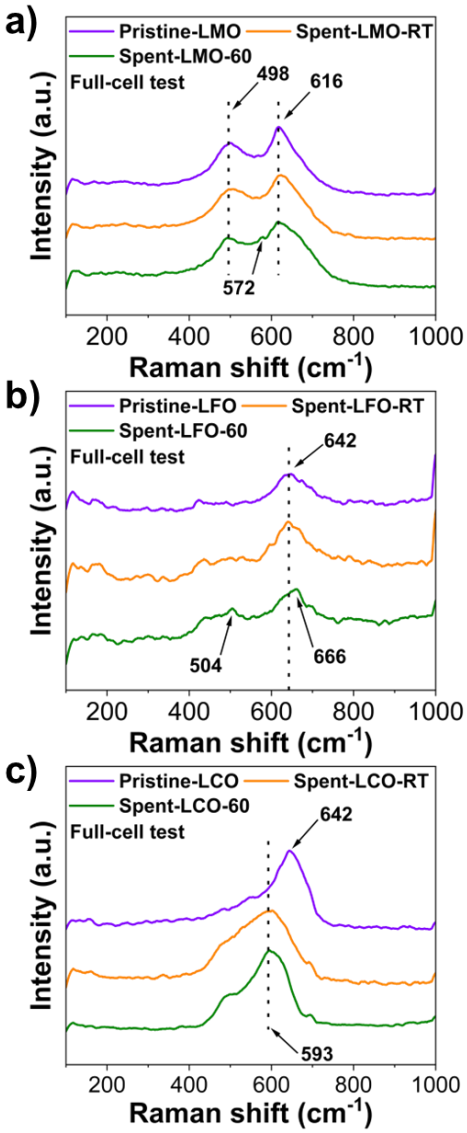

Figure 7. Raman spectroscopy data of LMO-, LFO-, and LCO-based electrodes (a, b, and c) before and after electrochemical testing in a zero-gap full-cell. Measurements were performed on pristine electrodes (magenta) and electrodes after full-cell testing at room temperature (spent-RT, orange) and 60 °C (spent-60, green).

2.5.2. Post-mortem XPS analysis of the thin films

XPS analysis of the LMO-based electrodes (Figure 8a-b, Figure S40a, Supporting Information) reveals that the La3d$_{5/2}$ spectra for the pristine-LMO sample and electrodes after full-cell testing at room temperature and 60 °C exhibit a multiplet peak split difference of 3.7 eV, characteristic of La-based perovskites.[27,28] The Mn2p$_{3/2}$ spectra after full-cell testing at room temperature and 60 °C show a shift from 641.6 to 642.1 eV toward higher binding energies. This shift is associated with an increased presence of Mn^{4+}, which aligns well with the Raman data.[70,71]

Additionally, O1s spectra across all samples indicate a reduction in $O_{lattice}$ and an increase in surface oxygen species.[72] For the LFO-based electrode, a slight narrowing of the $La3d_{5/2}$ multiplet distance is detected, decreasing from 3.8 eV in the pristine-LFO sample to 3.6 eV after full-cell testing at 60 °C (Figure S40b, Supporting Information). However, this value remains near the literature-reported 3.7 eV.[27,28] The $Fe2p_{3/2}$ demonstrates a significant change in the LFO-based electrode after full-cell testing at 60 °C compared to the other two LFO samples, as the peak emerges at 713.7 eV, which is associated with the increasing presence of Fe^{3+} on the surface (Figure 8c).[70,71] Similar to the case of LMO-based electrodes, O1s spectra of LFO-based samples suggest a rise in adsorbed oxygen species and a decrease in $O_{lattice}$ on the surface after electrochemical evaluation (Figure 8d). For LCO-based samples, the $La3d_{5/2}$ multiplet distance (Figure S40c, Supporting Information) is reduced from 3.8 to 3.5 eV, indicating the formation of $La(OH)_3$ on the electrode surface during OER.[65] This formation on the surface was also observed by Bai et al.,[65] who suggested that this is the main reason for the amorphization of LCO material. The $Co2p_{3/2}$ after full-cell testing at 60 °C (Figure 8e) displays an increase in Co^{3+}, as evidenced by a slight shift towards lower binding energies from 782.2 to 781.7 eV. This confirms the formation of a $CoO_x(OH)_y$.[65,66] Meanwhile, O1s spectra (Figure 8f) indicate an increase of adsorbed oxygen species on the surface and a decrease of metal oxides originating from the bulk, which is expected during water electrolysis. In general, XPS and Raman spectroscopy data show excellent agreement and correlate very well with the electrochemical data, which makes them ideal complementary techniques for future post-mortem analysis.

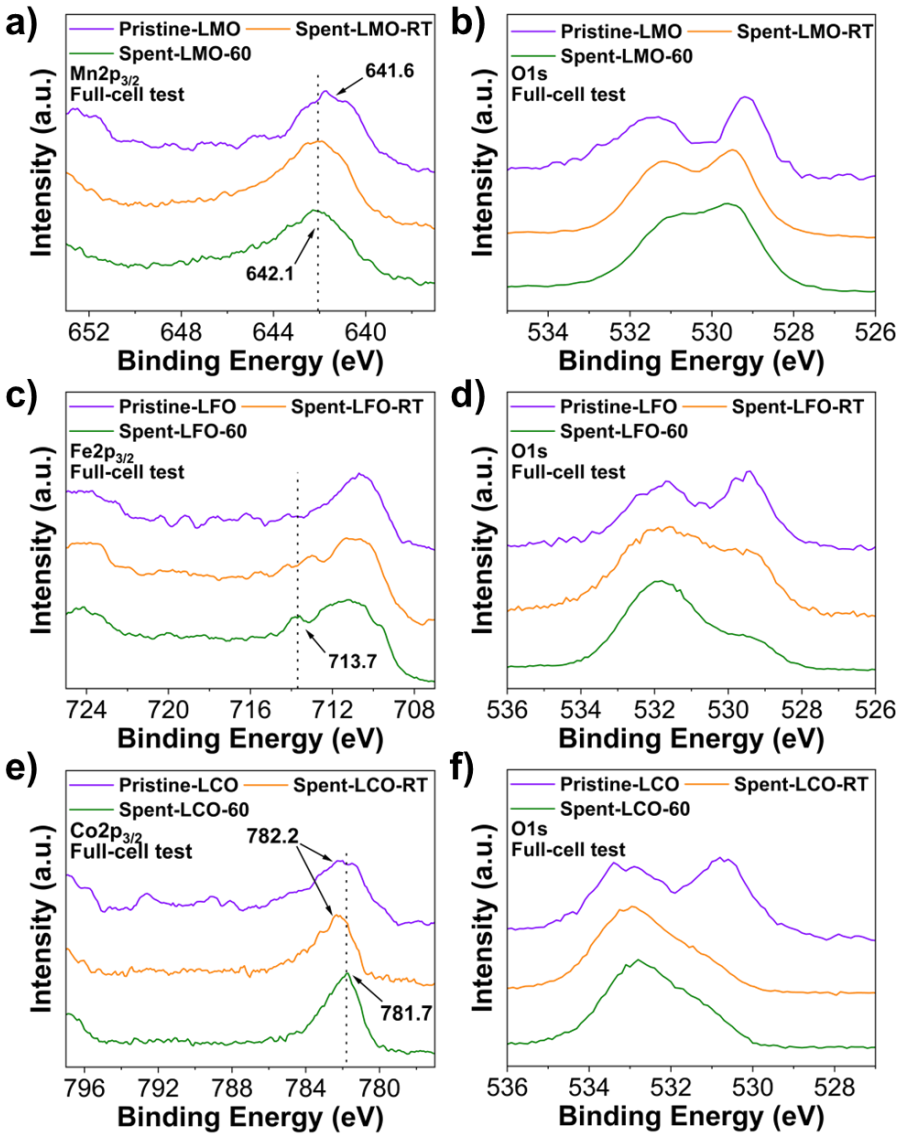

Figure 8. XPS data of $Mn2p_{3/2}$ and O1s on LMO-based electrodes(a, b). XPS data of $Fe2p_{3/2}$ and O1s on LFO-based electrodes (c, d). XPS data of $Co2p_{3/2}$ and O1s on LCO-based electrodes (e, f). Measurements are performed on pristine perovskite electrodes (magenta) and electrodes after full-cell testing at room temperature (spent-RT, orange) and at 60 °C (spent-60, green). All materials were exposed to a current density of 0.5 A cm^{-2}.

2.6. Post-mortem GIXRD analysis of the thin films

Additionally, GIXRD was performed on all three perovskite-based electrodes. As shown in Figure S41a–c (Supporting Information), the nickel substrate dominates the diffraction patterns, with distinct peaks at $2\theta = 44.5°$ and 52.9°. These correspond to the nickel foam and its non-flat nature. As a result, some of the catalytic material spills around the edges, leading to thinner material deposits on the surface and exposing more of the nickel substrate. In all cases, a gentle

peak is visible in the area between 2θ = 32° and 33°, which is connected to the perovskite structure. However, a closer examination reveals that LMO- and LFO-based electrodes after full-cell testing at room temperature and 60 °C exhibit no structural changes after exposure to harsh conditions, suggesting that these materials maintain robust structural integrity. However, in LCO-based electrodes, a peak shift after full-cell testing at 60 °C is detected towards lower 2θ values, which indicates the anodes' deformation in a crystalline structure. This observation aligns with the findings from Raman and XPS analysis. However, due to intense nickel peaks, a more detailed determination of the crystalline structure of LCO is not possible. Nonetheless, this shift indicates the presence of a mixture of phases within the LCO material.

In total, the combined results from post-mortem analyses, using Raman spectroscopy, XPS, and GIXRD, after electrochemical half-cell and full-cell testing reveal a direct link between the material's electrochemical performance and the observed materials properties. Notably, full-cell testing provides insights into the materials' behavior under realistic operating conditions that are not accessible through half-cell experiments alone. This integrated approach underscores the importance of evaluating electrode stability and reactivity at high current densities.

3. Conclusions

In this research, we investigated the effects of electrode material engineering on OER performance and emphasized the importance of the integration of scalable technologies and application-relevant testing into the material exploration process. By incorporating a structured, coherent workflow, we demonstrated a comprehensive strategy to evaluate La-based perovskites at different scales. This approach also accelerates knowledge transfer for the future development of next-generation electrocatalysts on relevant scales that are crucial to alleviating climate change. Based on our investigation, we can conclude:

- Firstly, perovskite nanopowders synthesized using spray-flame synthesis are highly crystalline, phase-pure materials with huge specific surface areas above 80 $m^2\ g^{-1}$. Their unique intrinsic properties provide a strong foundation for larger-scale catalyst production.
- Secondly, dispersion stability and ink formulation were proven as crucial factors for efficient and reproducible electrode preparation. All three nanomaterials demonstrate good dispersibility in ethanol. However, the dispersion stability decreases with increasing water-content in the continuous phase. Stability problems can be overcome by the incorporation of Sustainion® XA-9 binder, which significantly improves ink

stability and presents an important step towards a fluorine-free technology (per- and poly-fluoroalkyl substances – PFAS).

- Thirdly, morphological electrode evaluation revealed a correlation between the particle size after synthesis and the surface roughness of the electrodes, with LCO-based anodes exhibiting the highest roughness and porosity, which is connected to improved bubble management and exposure to active sites. Furthermore, coating homogeneity assessed using SDC shows low standard deviations, no delamination, and better OER performance of LFO-based anodes compared to the LCO-based material as reported in the literature.[7–9,11]
- Fourthly, electrochemical testing, including compression cell and RDE analysis, supports the SDC results and gives the first indications about the superior electrochemical performance of LFO- compared to LCO- and LMO-based electrodes. As the most important, all perovskites presented robust properties under laboratory testing conditions, which made them suitable candidates for further studies under real-life conditions in a zero-gap full-cell. Notably, full-cell testing at 60 °C revealed a change in OER performance due to a significant increase in the potential of the LFO-based sample, leading to a polarization-curve-crossing with the LCO-based electrode. Moreover, the LMO-based anode presents enhanced performance at high current densities compared to 10 mA cm^{-2}, indicating its potential as a toxic-metal-free OER electrocatalyst.
- Finally, we could strengthen the electrochemical observations with post-mortem analysis using Raman spectroscopy, XPS, and GIXRD, which enables investigations of materials stability and catalytic mechanisms. Changes in LMO-based anodes were linked to the increasing presence of Mn^{4+}, while LFO degradation correlated with iron leaching and increased Fe^{3+} concentration on the anode surface. In contrast, LCO-based anodes underwent structural changes connected to amorphization, resulting in enhanced long-term electrochemical stability.

Altogether, our findings contribute to the systematic exploration of perovskite-based OER electrocatalysts, where the faster integration of full-cell testing into the materials' assessment enhances our understanding of electrocatalyst behavior. We believe that these studies are needed to holistically understand electrocatalysts and enable bridging the gap between academia and industry. Notably, our results highlight the potential of gas-phase-synthesized perovskites using non-toxic, earth-abundant transitional metals such as iron and manganese. However, as presented, further development of electrocatalytic material stability and a deeper understanding

of the substrate effect on OER performance are needed to complete the whole picture of the effective electrode production for alkaline water electrolysis.

4. Experimental Section

Spray-flame synthesized perovskites: Nanomaterials applied for oxidation reaction tests were obtained by spray-flame synthesis. The setup consists of an in-house developed spray-flame reactor and a standardized SpraySyn burner,[73] which is well described in preceding publications.[74] The liquid precursor is composed of metal acetates – $La(CH_3CO_2)_3 \cdot 1.5\ H_2O$ (Alfa Aesar, 99.9 %), $Mn(CH_3CO_2)_2 \cdot 4\ H_2O$ (Sigma-Aldrich, 99 %), $Fe(acac)_3$ (Sigma-Aldrich, 99 %), and $Co(CH_3CO_2)_2 \cdot 4\ H_2O$ (Sigma-Aldrich, reagent grade) – which were dissolved in a mixture (35:65 vol.%) of ethanol and 2-ethylhexanoic acid. A precursor with a total metal ion concentration of 0.2 mol L^{-1} was transferred with a constant feed rate of 2 mL min^{-1} to the nozzle of the SpraySyn burner. In the nozzle, the precursor was brought into contact with the dispersion gas, a stream of mixed gases (1 standard liter per minute (slm) CH_4, 4.8 slm O_2), and formed a fine spray. To assure the stability of the flame and to avoid fluctuations in ignition, a premixed methane/oxygen flat flame (2 slm CH_4, 16 slm O_2) on a sintered bronze plate was used. The pilot flame was stabilized using a sheath gas flow (140 slm compressed air). An additional gas flow (240 slm compressed air) was used downstream of the flame for quenching and control of the off-gas temperature. The particles were precipitated on a fiber membrane filter and collected after synthesis was completed.

Characterization of perovskite nanopowders: A TEM and HRTEM (JEOL JEM 2200FS) using 120000- and 500000-times magnification equipped with EDX mapping was used to analyze the morphology, particle size, and elemental distribution. XRD patterns were recorded in the 2θ range from 10° to 90° (step size of 0.01°) using a Panalytical Empyrean diffractometer with Cu K_α (0.15406 nm) radiation. Raman spectroscopy measurements were performed using a Renishaw InVia Raman microscope equipped with 532 nm laser excitation (detection between 900 and 100 cm^{-1}). The XPS (ULVAC-PHI Versaprobe II, Chanhassen, USA) device was used to record powders applying an Al K_α radiation (hv = 1253.6 eV) with band-pass energy of 11.75 eV. As a reference, the XPS spectra were calibrated using the C1s adventitious carbon C–C binding energy at 284.8 eV. All spectra were analyzed with the CasaXPS 2.3.25 software. FTIR measurements were conducted using a spectrometer (Vertex 80, Bruker) between 4000 and 500 cm^{-1}. The N_2 adsorption measurements were performed using a Nova2000 device

(Anton Paar) to determine the specific surface area of the samples using the Brunauer-Emmett-Teller method.

Characterization of dispersions: To ensure the reproducibility of HSP values, procedures proposed by Süßet al., Bapat et al., and Anwar et al.[38,39,75] were employed. Dispersion stability measurements were performed using an analytical centrifuge (AC, LUM GmbH, Berlin, Germany) and were evaluated using transmission profiles and the AC software (SEPView 6.4.678.6069). The HSP sphere was determined using HSPiP software (5th Edition 5.4.08). Perovskite nanopowders were dispersed in different probe liquids with a 0.4 mg mL^{-1} concentration. Dispersions were prepared by sonication for 3 min using a sonication probe (Branson SFX 550 with a 3 mm sonication tip, 20% amplitude) in an ice bath. The energy input characteristics during the sonication process were obtained based on recommendations outlined in the NanoREG D4.12 SOP (Figure S42, Supporting Information). Subsequently, 440 µL of the as-prepared dispersion was transferred into 2 mm AC cells and inserted into the AC. The measurements were carried out at 2000 rpm, 25 °C, and a wavelength of 410 nm.

Construction of catalyst electrodes on nickel plates and nickel foam: Inks composed of active materials in a concentration of 1 mg mL^{-1} were deposited onto nickel plates (purity: 99.2 %, HMW Hauner, 1×1 cm^2) and nickel foam (porosity: 95 %, purity 99.9 %, diameter: 4 cm, Goodfellow) using an ultrasonic spray coating system (Prism^{TM} 400 Ulra-Coat, USI Ultrasonic Systems Inc.). Before the coating process, the nickel substrates underwent cleaning using an ultrasonic bath (Elmasonic S, Elma) in Milli-Q water (Millipore purification system), 1 mol L^{-1} HCl, and acetone. The catalysts ink (40 mg) were prepared by 5 minutes of sonication (Branson SFX 550 using a 3 mm sonication tip, 20% amplitude) in 40 mL of water/ethanol mixture (75/25 v%). Subsequently, Sustainion® XA-9 ionomer (5 wt% in ethanol, Dioxide Materials) was added to the catalyst dispersion (concentration 5 µL of Sustainion® per mg of catalyst material), followed by further sonication for 5 min in an ice bath. The resulting ink was sprayed over a nickel substrate heated to 150 °C in 40 coating runs, with an interval of 5 s between each consecutive spray. The final mass loading of the catalyst on the anode support was 250 µg cm^{-2}, determined gravimetrically.

Flow cell coupled with Inductively Coupled Plasma Optical Emission Spectroscopy (ICP-OES): Inks composed of active materials were deposited onto polished nickel plates, polished Nickel RDE disks (purity: 99.2%, HMW Hauner, 0.5x0.5 cm), and polished glassy-carbon

plates (purity 99.9%, 0.5x0.5 cm) using an ultrasonic spray coating system (Sono-Tek Corporation). Before the coating process, the nickel substrates underwent cleaning using an ultrasonic bath (Elamsonic S, Elma) in Milli-Q water (18.2 MΩ cm), 1 mol L^{-1} HCl, and acetone. Meanwhile, glassy carbon substrates were cleaned using an ultrasonic bath (Elmasonic S, Elma) in Milli-Q water (18.2 MΩ cm), 2-propanol, and acetone. The catalyst inks (20 mg) were prepared by 3 minutes of sonication (Branson SFX 550 using a 3 mm sonication tip, 20 % amplitude) in 20 mL of water/ethanol mixture (75/25 v%). Subsequently, Sustainion® XA-9 ionomer (5 wt% in ethanol, Dioxide Materials) was added to the catalyst dispersion (concentration 5 µL of Sustainion® per mg of catalyst material), followed by further sonication for 3 min in an ice bath. The resulting ink was sprayed over substrates heated to 150 °C in 160 coating runs, with an interval of 5 s between each consecutive spray. The final mass loading of the catalyst on the anode support was 1 mg cm^{-2}, determined gravimetrically.

Characterization of catalyst electrodes: The anodes' morphology was examined by SEM (Nanoprobe 710, Ulvac-Phi) using an acceleration voltage of 5 kV and EDX (Quantax, Bruker) using an acceleration voltage of 20 kV. The morphology of the fabricated coatings was additionally inspected using AFM (30 x 30 µm, Tosca 400, Anton Paar). All topography measurements were conducted in non-contact mode using an AFM probe (ARROW-NCR-20) and analyzed with the Tosca Analysis 7.4 software. XRD patterns were recorded in the 2θ range from 15° to 80° (step size of 0.07°, compression cell) and from 20° to 70° (step size of 0.07°, full-cell) using a Rigaku Smartlab diffractometer with Cu K_α (0.15406 nm) radiation in grazing incidence mode (GIXRD). Raman spectroscopy measurements on electrode surfaces were performed using a Renishaw InVia Raman microscope equipped with 532 nm laser excitation (between 900 and 100 cm^{-1}, 77mW). The XPS spectra of perovskites coated on nickel foam were recorded using the (ULVAC-PHI Versaprobe II, Chanhassen, USA) device applying an Al Kα radiation (hv = 1253.6 eV) with a band-pass energy of 11.75 eV. As a reference, the XPS spectra were calibrated using the C1s adventitious carbon C–C binding energy at 284.8 eV. Subsequently, the resulting XPS spectra were analyzed using CasaXPS 2.3.25 software, with fitting carried out using a Shirley-type background and a Lorentzian lineshape. Contact angle measurements were performed using 1 mol L^{-1} purified KOH using a Dataphysics Contact Angle System OCA.

4.1. Electrochemistry

A standard protocol was employed for all electrochemical experiments to enable the comparison between the various electrocatalytic cells. The 1 mol L^{-1} KOH electrolyte was prepared using Milli-Q water with a resistivity of 18.2 MΩ cm and was further purified of metal cations using a Chelex®100 cation-exchange resin (Sigma Aldrich). All half-cell experiments were performed in O_2-saturated electrolyte at room temperature, while in the zero-gap full-cell, application-relevant conditions were simulated. All potential values measured in this study were converted to a reversible hydrogen electrode (RHE) scale using Equation (1).

$$E_{iR}(\mathrm{RHE}) = E_{\mathrm{Ag/AgCl}} + E^{0}_{\mathrm{Ag/AgCl}} + 0.059 \cdot \mathrm{pH} - iR \quad (1)$$

Where E_{iR} (RHE) is the electrode potential compensated for the iR-drop in the RHE scale (V vs. RHE), $E_{\mathrm{Ag/AgCl}}$ is the measured potential versus Ag/AgCl (3.4 mol L^{-1} KCl, in V), and $E^{0}_{\mathrm{Ag/AgCl}}$ is the standard potential of the Ag/AgCl (3.4 mol L^{-1} KCl) reference electrode (0.21 V). The potentials were 85% automatically and 15 % manually *iR*-corrected using the uncompensated resistance (R, Ω), which was calculated by potentiostatic electrochemical impedance spectroscopy (PEIS) in the high-frequency range.[13]

Scanning droplet cell: The electrochemical measurement of the Ni-plates coated with three different catalysts was executed using a high-throughput SDC purchased from Sensolytics GmBH, coupled with a Metrohm Autolab PGSTAT204 bipotenstiostat/galvanostat. The SDC electrochemical cell is composed of a three-electrode system, with a Pt coil as the counter electrode, an Ag/AgCl (3.4 mol L^{-1} KCl) as the reference electrode, and the working electrode formed upon contact of the SDC PTFE tip with the coated Ni-plate. The SDC cell is coupled to a force sensor and is mounted on robotic arms for sealing and precise positioning of the cell over the electrode surface. Fresh electrolyte (O_2-saturated, 1 mol L^{-1} purified KOH) was provided for every measured area via a piston pump connected with PTFE tubes to the SDC cell. Before each measurement, the opening area of the PTFE tip of the SDC cell was measured with an optical microscope Di-Li 955 (Distelkamp). At each 1×1 cm^2 electrode, the electrochemical activity of the catalyst was measured at 25 individual spots, according to the following protocol: Initially, the open circuit potential (OCP) was recorded for 60 s. Afterward, 50 cyclic voltammograms were recorded (CV) with 100 mV s^{-1} in a potential range of 0.0 to

1.40 V vs. RHE. Subsequently, a linear sweep voltammogram (LSV) was recorded from 0.0 to 1.8 V vs. RHE with 5 mV s^{-1} with a stop-criterion of 50 µA. Lastly, electrochemical impedance spectroscopy (EIS) was measured at 0.0 V vs. OCP for 60 s, in a frequency range from 100 kHz to 1 Hz at 10 step dec^{-1}, with a sine wave of 10 mV (RMS) AC amplitude.[13] Statistical analyses of the current densities and overpotentials between the coated electrodes were evaluated using an ANOVA test by Past 4.0 software, with a level of significance set at a *p*-value ($p < 0.05$).

Rotating Disk Electrode: The RDE experiments were performed with a VSP-3e bipotentiostat (BioLogic, France) and a RDE rotator (PINE research, model: AFMSRCE, USA). Both polycrystalline nickel electrode (Ni – Ageo = 0.196 cm^2) and glassy carbon (GC – Ageo = 0.196 cm^2) electrodes (PINE research) were used as working electrode (WE), RHE (HydroFlex─Gaskatel) and a glassy carbon rod (HTW Hochtemperatur-Werkstoffe GmbH) and were used as a reference electrode (RE) and a counter (CE), respectively. Catalyst inks of 5 mg mL^{-1} were drop cast on the fresh polished electrode surface (using alumina powder following 1.0, 0.3, and 0.05 µm grain size) with a catalyst mass loading of 1 mg cm^{-2}. Afterwards, the electrodes were dried at room temperature for at least 60 min. The electrochemical protocol was based on the work.[13] EIS spectra were recorded at OCP and 1.60 V vs. RHE applying a 10 mV sinewave from 30 kHz to 1 Hz, 10 step dec^{-1} to determine the uncompensated resistance for both iR-drop correction and charge transfer resistance, respectively. During the RDE measurement, 85 % *iR*-drop correction was applied automatically by the software EC-Lab. The remaining 15 % *iR*-drop correction was post-processed in OriginLab 2022.

Compression cell: Electrochemical measurements under a homogeneous potential distribution were performed using a compression cell.[13,57] A commercial hydrogen electrode (Gaskatel) was used as a reference electrode. To ensure its potential stability, the reference electrode was tested against a $Hg/HgSO_4$ (Na_2SO_4 sat.) before and after each experiment. Platinum mesh 1 × 3 cm^2 parallel to the working electrode as a counter electrode, and the Ni foil coated with the catalysts electrode used as a working electrode. The electrochemical protocol used was as follows: The electrode was stabilized by taking 50 CVs with a scan rate of 100 mV s^{-1} from 0.0 to 1.4 V vs. RHE. LSV at a scan rate of 5 mV s^{-1} was used to evaluate the electrochemical behavior, whereas chronopotentiometry with a current density of 10 mA cm^2 was used to investigate the electrochemical stability. EIS at OCP, from 30 kHz to 1 Hz, was performed and the spectra were fitted to the appropriate EEC to obtain the uncompensated resistance for iR-

drop correction. Electrochemical and impedance spectra were collected using a computer-controlled VSP-300 potentiostat (BioLogic).

Flow cell coupled with ICP-OES: The electrochemical characterization of the catalyst-coated substrates was performed using a flow cell combined with an ICP-OES. The ICP flow rate was either 1.5 or 4 mL min^{-1}. Standard solutions for La, Mn, and Co were prepared by diluting the ICP standard (Sigma-Aldrich) using 1 mol L^{-1} KOH. A leak-free Ag/AgCl (3.4M KCl) electrode (innovative instruments)) was used as the reference electrode, and a Pt coil was used as the counter electrode. In the closed-type flow cell, a polypropylene separator membrane (Celgard 3401) was used. The membrane separating the working and counter-electrode compartments of the cell, together with the O-rings, was replaced every few weeks as the polymer stretched to ensure that contamination did not build up. New membranes were punched out using a 10 mm diameter punch and die. The cell was periodically disassembled and placed in an acid bath of 2–5 % nitric acid for a few hours before being thoroughly rinsed with Milli-Q water (18.2 MΩ cm). Downstream of the working electrode, PTFE tape was sometimes used to replace Delrin ferrules with similar results. Parafilm was also found to be very effective as a ferrule material. The counter electrode was replenished each day of the experiment with 1 mol L^{-1} KOH. Otherwise, pH differences between the counter electrode compartment and the flow compartment could increase due to CO_2 absorption from alkaline solutions.

Full cell test: The experiments were carried out in a custom-made two-electrode zero-gap cell using a Gamry Reference 3000 potentiostat equipped with a Booster (Gamry) unit. For the anode side, a 0.40 mm thick PTFE sealing and for the cathode side, a 0.15 mm thick PTFE sealing was used. The membrane electrode assembly (MEA) applied in the full-cell measurements consisted of the individual catalyst-coated nickel foams (40 mm diameter, 0.4 mm thickness) as an anode, and a PiperION-HCO3 membrane (40 µm thickness) conditioned for at least 24 h in 1 mol L^{-1} KOH as anion exchange membrane and an H23 (Freudenberg) carbon paper coated with platinum, nominally 40 % on carbon black (2.9 mg cm^{-2}, 1.0 mg Pt cm^{-2}) loading, 10 wt% Sustainion® XA-9 binder, 40 mm diameter, 0.15 mm thickness) applied with an Eclipse Airbush pistol (Iwata). This placement is crucial for minimizing the contribution of cell resistance arising from both the electrolyte and the formation of bubbles during oxygen and hydrogen evolution. The voltage in the electrochemical cell depends on the spacing between the electrodes, where the gapless system promotes high efficiencies.[76] Prior to applying the platinum to the carbon paper, which was heated to 110 °C

on a hotplate, the ink was ultrasonicated for 10 min (VWR USC-T, ultrasonic frequency approx. 45 kHz) and afterward further dispersed using a T-25 Ultra-Turrax operating at 13400 rpm for 2 mins. The cathode consisted of 1.0 mg cm^{-2} of platinum. The dry weight of the catalyst also included 10 wt% Sustainion® XA-9 binder (Dioxide Materials), which was added as 5 wt% dispersion in ethanol to an ink consisting of 6:1 volumes of isopropanol and water. The Ni-foam anodes (porosity: 95%, purity: 99.9%, Goodfellow) were compressed from 1.6 mm thickness to 0.4 mm using a hydraulic press before coating. For the polarization curve measurements, 20 s long multi-step chronopotentiometries held at the corresponding current densities were recorded. Before the 12 h chronopotentiometries held at 0.5 A cm^{-2} were initiated, a 1 h conditioning at the same current density was performed.

Acknowledgments

B.T. gratefully acknowledges a scholarship from the International Max Planck Research School (IMPRS) RECHARGE doctoral program. A.R.K. acknowledges the support of a Ph.D. fellowship awarded by the Higher Education Commission (HEC) of Pakistan and the German Academic Exchange Service (DAAD). K.Y.M. acknowledges Petroleum Technology Development Fund (PTDF), Nigeria for doctoral fellowship with Pef No.: PTDF/ED/OSS/PHD/KYM/1723/20 and ID: 20PHD031.The authors acknowledge funding by the German Research Foundation (DFG) within the CRC/TRR 247 (Heterogeneous Oxidation Catalysis in the Liquid Phase 388390466), the Mercator Research Center Ruhr within the DIMENSION project (MERCUR.Exzellenz, 'DIMENSION' Ex-2021-0034). D.S., H.H., C.S., C.A., and U.-P.A. would also like to acknowledge the Ministry of Culture and Science of the State of North Rhine-Westphalia (Materials for Future Hydrogen Technologies – Mat4Hy) support. All contributors acknowledge MAT4HY.NRW Consortium for cooperative support. C.A. acknowledges funding by the Ministry of Culture and Science of the State of North Rhine-Westphalia (PB NRW 2022 - Application 19). The authors also gratefully acknowledge the support from the Interdisciplinary Center for Analytics on the Nanoscale (ICAN), a core facility at the University of Duisburg-Essen. The nanopowder X-Ray data were collected using Panalytical Empyrean. We would like to thank D.C.L. for assistance in using the instrument. The electrode X-ray data were collected using the Rigaku Smartlab High-Resolution diffractometer of the Nanoparticle Processing Technology (NPPT) group at the University of Duisburg-Essen. The instrument is funded through the DFG Instrument proposal INST

20876/395-1 FUGG project number 450350889 and the state of North Rhine-Westphalia, Germany. We would like to thank M.S. for assistance in using the instrument.

Conflict of Interests

The authors declare no conflict of interest.

Data Availability Statement

The data that support the findings of this study are openly available at Zenodo at 10.5281/zenodo.15348465.

Received: ((will be filled in by the editorial staff))
Revised: ((will be filled in by the editorial staff))
Published online: ((will be filled in by the editorial staff))

References

[1] a) S. Anantharaj, S. R. Ede, K. Sakthikumar, K. Karthick, S. Mishra, S. Kundu, *ACS Catal.* **2016**, *6*, 8069; b) B. Mohanty, P. Bhanja, B. K. Jena, *Materials Today Energy* **2022**, *23*, 100902.

[2] a) J. X. Flores-Lasluisa, F. Huerta, D. Cazorla-Amorós, E. Morallón, *Energy* **2023**, *273*, 127256; b) A. Ashok, A. Kumar, J. Ponraj, S. A. Mansour, F. Tarlochan, *Catalysis Today* **2021**, *375*, 484; c) M. S. Alom, C. C. W. Kananke-Gamage, F. Ramezanipour, *ACS omega* **2022**, *7*, 7444; d) J. Suntivich, K. J. May, H. A. Gasteiger, J. B. Goodenough, Y. Shao-Horn, *Science (New York, N.Y.)* **2011**, *334*, 1383.

[3] J. A. Dias, M. A. S. Andrade, H. L. S. Santos, M. R. Morelli, L. H. Mascaro, *ChemElectroChem* **2020**, *7*, 3173.

[4] a) A. Mendoza, O. Guzmán in *Recent Advances in Multifunctional Perovskite Materials* (Eds.: P. Sharma, A. Kumar), IntechOpen, **2022**; b) J. Chen, M. Shen, X. Wang, G. Qi, J. Wang, W. Li, *Applied Catalysis B: Environmental* **2013**, *134-135*, 251.

[5] Z. Jia, C. Cheng, X. Chen, L. Liu, R. Ding, J. Ye, J. Wang, L. Fu, Y. Cheng, Y. Wu, *Mater. Adv.* **2023**, *4*, 79.

[6] Y. Wang, Y. Wang, X. Liu, Y. Guo, Y. Guo, G. Lu, *Journal of nanoscience and nanotechnology* **2009**, *9*, 933.

[7] A. Ashok, A. Kumar, R. R. Bhosale, F. Almomani, S. S. Malik, S. Suslov, F. Tarlochan, *Journal of Electroanalytical Chemistry* **2018**, *809*, 22.

[8] M. V. Kante, M. L. Weber, S. Ni, I. C. G. van den Bosch, E. van der Minne, L. Heymann, L. J. Falling, N. Gauquelin, M. Tsvetanova, D. M. Cunha et al., *ACS nano* **2023**, *17*, 5329.

[9] T. X. Nguyen, Y.-C. Liao, C.-C. Lin, Y.-H. Su, J.-M. Ting, *Adv Funct Materials* **2021**, *31*.

[10] R. Xie, Z. Nie, X. Hu, Y. Yu, C. Aruta, N. Yang, *ACS Appl. Energy Mater.* **2021**, *4*, 9057.

[11] J. X. Flores-Lasluisa, F. Huerta, D. Cazorla-Amorós, E. Morallon, *Nanomaterials (Basel, Switzerland)* **2020**, *10*.

[12] a) M. M. Rashad, E. M. Elsayed, M. M. Moharam, R. M. Abou-Shahba, A. E. Saba, *Journal of Alloys and Compounds* **2009**, *486*, 759; b) F. Li, J. Ran, M. Jaroniec, S. Z. Qiao, *Nanoscale* **2015**, *7*, 17590.

[13] P. Gerschel, S. Angel, M. Hammad, A. Olean-Oliveira, B. Toplak, V. Chanda, R. Martínez-Hincapié, S. Sanden, A. R. Khan, Da Xing et al., *Carbon Energy* **2024**.

[14] M. Hammad, S. Angel, A. K. Al-Kamal, A. Asghar, M.-A. Kräenbring, A. Amin, H. T. Wiedemann, A. S. Amin, V. Vinayakumar, T. C. Schmidt et al., *Process Safety and Environmental Protection* **2025**, *194*, 1347.

[15] S. Angel, J. D. Tapia, J. Gallego, U. Hagemann, H. Wiggers, *Energy Fuels* **2021**, *35*, 4367.

[16] a) L. Grebener, A. S. Odungat, Y. Zhu, O. Pasdag, I. Radev, E. Nürenberg, A. Kubina, V. Peinecke, S. Kohsakowski, D. Segets et al., *Journal of Power Sources* **2025**, *635*, 236457; b) A. Jain, C. Marcks, L. Grebener, J. Johny, A. S. Odungat, M. Chatwani, M.-A. Kräenbring, A. Shaji, M. F. Tesch, A. K. Mechler et al., *Adv Funct Materials* **2025**.

[17] a) M. Pidburtnyi, B. Zanca, C. Coppex, S. Jimenez-Villegas, V. Thangadurai, *Chem. Mater.* **2021**, *33*, 4249; b) Z. Shen, Y. Zhuang, W. Li, X. Huang, F. E. Oropeza, E. J. M. Hensen, J. P. Hofmann, M. Cui, A. Tadich, D. Qi et al., *J. Mater. Chem. A* **2020**, *8*, 4407; c) Y. Zhu, W. Zhou, J. Yu, Y. Chen, M. Liu, Z. Shao, *Chem. Mater.* **2016**, *28*, 1691; d) Y. D. Susanti, N. Afifah, R. Saleh, *IOP Conf. Ser.: Mater. Sci. Eng.* **2019**, *496*, 12037.

[18] a) S. Thirumalairajan, K. Girija, N. Y. Hebalkar, D. Mangalaraj, C. Viswanathan, N. Ponpandian, *RSC Adv.* **2013**, *3*, 7549; b) S. Zhou, X. Miao, X. Zhao, C. Ma, Y. Qiu, Z. Hu, J. Zhao, L. Shi, J. Zeng, *Nature communications* **2016**, *7*, 11510.

[19] M. N. Iliev, M. V. Abrashev, H.-G. Lee, V. N. Popov, Y. Y. Sun, C. Thomsen, R. L. Meng, C. W. Chu, *Phys. Rev. B* **1998**, *57*, 2872.

[20] M. V. Abrashev, A. P. Litvinchuk, M. N. Iliev, R. L. Meng, V. N. Popov, V. G. Ivanov, R. A. Chakalov, C. Thomsen, *Phys. Rev. B* **1999**, *59*, 4146.

[21] A. F. Manchón-Gordón, P. E. Sánchez-Jiménez, J. S. Blázquez, A. Perejón, L. A. Pérez-Maqueda, *Materials (Basel, Switzerland)* **2023**, *16*.

[22] Y. Huang, J. Liu, D. Cao, Z. Liu, K. Ren, K. Liu, A. Tang, Z. Wang, L. Li, S. Qu et al., *International Journal of Hydrogen Energy* **2019**, *44*, 13242.

[23] M. Połomska, B. Hilczer, J. Wolak, A. Pietraszko, M. Balcerzak, M. Jurczyk, J. Jakubowicz, *Phase Transitions* **2014**, *87*, 909.

[24] L. Tepech-Carrillo, A. Escobedo-Morales, A. Pérez-Centeno, E. Chigo-Anota, J. F. Sánchez-Ramírez, E. López-Apreza, J. Gutiérrez-Gutiérrez, *Journal of Nanomaterials* **2016**, *2016*, 1.

[25] Y.-P. Zhang, H.-F. Liu, H.-L. Hu, R.-S. Xie, G.-H. Ma, J.-C. Huo, H.-B. Wang, *Royal Society open science* **2018**, *5*, 171376.

[26] H. A. Martinez-Rodriguez, K. Onyekachi, A. Concha-Balderrama, G. Herrera-Pérez, J. A. Matutes-Aquino, J. F. Jurado, M. H. Bocanegra-Bernal, V.-H. Ramos-Sánchez, J. A. Duarte-Moller, A. Reyes-Rojas, *Journal of Alloys and Compounds* **2020**, *816*, 152668.

[27] D. Çoban Özkan, A. Türk, E. Çelik, *J Mater Sci: Mater Electron* **2020**, *31*, 22789.

[28] J. X. Flores-Lasluisa, F. Huerta, D. Cazorla-Amorós, E. Morallón, *Energy* **2022**, *247*, 123456.

[29] G. Fang, K. Liu, M. Fan, J. Xian, Z. Wu, L. Wei, H. Tian, H. Jiang, W. Xu, H. Jin et al., *Carbon Neutralization* **2023**, *2*, 709.

[30] M. Wang, B. Han, J. Deng, Y. Jiang, M. Zhou, M. Lucero, Y. Wang, Y. Chen, Z. Yang, A. T. N'Diaye et al., *ACS applied materials & interfaces* **2019**, *11*, 5682.

[31] M. Hammad, S. Angel, A. K. Al-Kamal, A. Asghar, A. Said Amin, M.-A. Kräenbring, H. T. Wiedemann, V. Vinayakumar, M. Yusuf Ali, P. Fortugno et al., *Chemical Engineering Journal* **2023**, *454*, 139900.

[32] a) R. Wang, C. Ye, H. Wang, F. Jiang, *ACS omega* **2020**, *5*, 30373; b) M. Khalifa, A. M. El Sayed, S. M. Kassem, E. Tarek, *Scientific reports* **2024**, *14*, 3672.

[33] S. Abbot, *Solubility Science: Principles and Practice*, Creative Commons BY-ND, **2017**.

[34] O. Anwar, S. Bapat, J. Ahmed, X. Xie, J. Sun, D. Segets, *Nanoscale* **2022**, *14*, 13593.

[35] A. S. Amin, D. Lerche, A. S. Odungat, S. U. Boehm, T. Koch, F. Özcan, D. Segets, *ChemCatChem* **2024**.

[36] S. Bapat, D. Segets, *ACS Appl. Nano Mater.* **2020**, *3*, 7384.

[37] O. Anwar, A. S. Amin, A. Amin, M.-A. Kräenbring, F. Özcan, D. Segets, *Part & Part Syst Charact* **2023**, *40*.

[38] S. Süß, T. Sobisch, W. Peukert, D. Lerche, D. Segets, *Advanced Powder Technology* **2018**, *29*, 1550.

[39] a) S. Khandavalli, J. H. Park, N. N. Kariuki, D. J. Myers, J. J. Stickel, K. Hurst, K. C. Neyerlin, M. Ulsh, S. A. Mauger, *ACS applied materials & interfaces* **2018**, *10*, 43610; b) L. de Sousa, C. Harmoko, N. Benes, G. Mul, *ACS EST Eng.* **2021**, *1*, 1649.

[40] Z. Xu, J. Liang, L. Zhou, *Journal of Alloys and Compounds* **2013**, *546*, 112.

[41] G. Mladin, M. Ciopec, A. Negrea, N. Duteanu, P. Negrea, P. Ianasi, C. Ianași, *Materials (Basel, Switzerland)* **2022**, *15*.

[42] G. M. Estrada-Villegas, G. Morselli, M. J. A. Oliveira, G. González-Pérez, A. B. Lugão, *Polym. Bull.* **2020**, *77*, 4147.

[43] A. Taheri Najafabadi, A. A. Khodadadi, M. J. Parnian, Y. Mortazavi, *Applied Catalysis A: General* **2016**, *511*, 31.

[44] T.-D. Hoang, N. Nghiem, *Fermentation* **2021**, *7*, 314.

[45] E. Newes, C. Clark, L. Vimmerstedt, S. Peterson, D. Burkholder, D. Korotney, D. Inman, *Energy policy* **2021**, *161*, 1.

[46] a) J. Areola Hernandez, G. S. Uddin, A. Dutta, A. Ahmed, S. H. Kang, *Physica A: Statistical Mechanics and its Applications* **2020**, *551*, 124094; b) A. Bastianin, M. Galeotti, M. Manera, *Energy Economics* **2014**, *42*, 152; c) P. H. Hoeckel, A. M. Alvim, J. P. Pontes, J. Dias, *Energies* **2023**, *16*, 2788; d) A. S. Nascimento Filho, H. Saba, R. G. O. dos Santos, J. G. A. Calmon, M. L. V. Araújo, E. M. F. Jorge, T. B. Murari, *Sustainability* **2021**, *13*, 9899; e) T. Mizik, L. Nagy, Z. Gabnai, A. Bai, *Energies* **2020**, *13*, 5614.

[47] a) K. Guan, J. Shen, G. Liu, J. Zhao, H. Zhou, W. Jin, *Separation and Purification Technology* **2017**, *174*, 126; b) Y. Luo, J. Zhang, Z. Zhou, J. P. Aguilar-Lopez, R. Greco, T. Bogaard, *Hydrol. Earth Syst. Sci.* **2023**, *27*, 783.

[48] J. Islam, B. S. Yoon, P. T. Thien, C. H. Ko, S.-K. Kim, *Catalysis Today* **2024**, *425*, 114349.

[49] Y. Li, Z. Kan, L. Jia, D. Zhang, Y. Hong, J. Liu, H. Huang, S. Li, S. Liu, *Trans. Tianjin Univ.* **2023**, *29*, 313.

[50] K. Tsuburaya, K. Obata, K. Nagato, K. Takanabe, *ACS Sustainable Chem. Eng.* **2024**, *12*, 16308.

[51] a) A. Vazhayil, J. Thomas, N. Thomas, *Journal of Electroanalytical Chemistry* **2022**, *918*, 116426; b) X. Liu, H. Gong, T. Wang, H. Guo, L. Song, W. Xia, B. Gao, Z. Jiang, L. Feng, J. He, *Chemistry, an Asian journal* **2018**, *13*, 528.

[52] a) W. G. Hardin, J. T. Mefford, D. A. Slanac, B. B. Patel, X. Wang, S. Dai, X. Zhao, R. S. Ruoff, K. P. Johnston, K. J. Stevenson, *Chem. Mater.* **2014**, *26*, 3368; b) H. He, J. Chen, D. Zhang, F. Li, X. Chen, Y. Chen, L. Bian, Q. Wang, P. Duan, Z. Wen et al., *ACS Catal.* **2018**, *8*, 6617.

[53] Yun Bao, Kensaku Nagasawa, Yoshiyuki Kuroda, Shigenori Mitsushima, *Electrocatalysis* **2020**, *11*, 301.

[54] A. R. C. Bredar, A. L. Chown, A. R. Burton, B. H. Farnum, *ACS Appl. Energy Mater.* **2020**, *3*, 66.

[55] V. Tripkovic, H. A. Hansen, J. M. Garcia-Lastra, T. Vegge, *J. Phys. Chem. C* **2018**, *122*, 1135.

[56] R. Martínez-Hincapié, J. Wegner, M. U. Anwar, A. Raza-Khan, S. Franzka, S. Kleszczynski, V. Čolić, *Electrochimica Acta* **2024**, *476*, 143663.

[57] E. Budiyanto, S. Salamon, Y. Wang, H. Wende, H. Tüysüz, *JACS Au* **2022**, *2*, 697.

[58] J. Knöppel, M. Möckl, D. Escalera-López, K. Stojanovski, M. Bierling, T. Böhm, S. Thiele, M. Rzepka, S. Cherevko, *Nature communications* **2021**, *12*, 2231.

[59] L. An, R. Chen, Y. Li (Eds.) *Green Energy and Technology*, Springer International Publishing; Imprint Springer, Cham, **2023**.

[60] a) R. Baddour-Hadjean, J.-P. Pereira-Ramos, *Chemical reviews* **2010**, *110*, 1278; b) H. R. Barai, A. N. Banerjee, S. W. Joo, *Journal of Industrial and Engineering Chemistry* **2017**, *56*, 212.

[61] a) N. S. Chaudhari, S. S. Warule, S. Muduli, B. B. Kale, S. Jouen, B. Lefez, B. Hannoyer, S. B. Ogale, *Dalton transactions (Cambridge, England : 2003)* **2011**, *40*, 8003; b) S. P. Schwaminger, P. Fraga-García, F. Selbach, F. G. Hein, E. C. Fuß, R. Surya, H.-C. Roth, S. A. Blank-Shim, F. E. Wagner, S. Heissler et al., *Adsorption* **2017**, *23*, 281.

[62] C. Pasquini, L. D'Amario, I. Zaharieva, H. Dau, *The Journal of chemical physics* **2020**, *152*, 194202.

[63] J. Huang, H. Sheng, R. D. Ross, J. Han, X. Wang, B. Song, S. Jin, *Nature communications* **2021**, *12*, 3036.

[64] F. Bai, J. Schulwitz, T. Priamushko, U. Hagemann, A. Kostka, M. Heidelmann, S. Cherevko, M. Muhler, T. Li, *Journal of Catalysis* **2024**, *438*, 115697.

[65] W. Hu, Q. Liu, T. Lv, F. Zhou, Y. Zhong, *Electrochimica Acta* **2021**, *381*, 138276.

[66] Z. Li, Y. Xie, Z. Huang, Y. Su, C. Sun, J. Fu, H. Wei, F. Wu, G. Ou, *ACS Appl. Nano Mater.* **2022**, *5*, 14209.

[67] W. Cai, R. Chen, H. Yang, H. B. Tao, H.-Y. Wang, J. Gao, W. Liu, S. Liu, S.-F. Hung, B. Liu, *Nano letters* **2020**, *20*, 4278.

[68] A. Indra, P. W. Menezes, N. R. Sahraie, A. Bergmann, C. Das, M. Tallarida, D. Schmeißer, P. Strasser, M. Driess, *Journal of the American Chemical Society* **2014**, *136*, 17530.

[69] J. Wang, X. Ma, F. Qu, A. M. Asiri, X. Sun, *Inorganic chemistry* **2017**, *56*, 1041.

[70] F. Bao, E. Kemppainen, I. Dorbandt, F. Xi, R. Bors, N. Maticiuc, R. Wenisch, R. Bagacki, C. Schary, U. Michalczik et al., *ACS Catal.* **2021**, *11*, 10537.

[71] C. Lv, H. Chen, M. Hu, T. Ai, H. Fu, *Environmental science and pollution research international* **2021**, *28*, 37142.

[72] F. Schneider, S. Suleiman, J. Menser, E. Borukhovich, I. Wlokas, A. Kempf, H. Wiggers, C. Schulz, *The Review of scientific instruments* **2019**, *90*, 85108.

[73] a) C. Schulz, T. Dreier, M. Fikri, H. Wiggers, *Proceedings of the Combustion Institute* **2019**, *37*, 83; b) S. Hardt, I. Wlokas, C. Schulz, H. Wiggers, *Journal of nanoscience and nanotechnology* **2015**, *15*, 9449.

[74] S. Bapat, C. Giehl, S. Kohsakowski, V. Peinecke, M. Schäffler, D. Segets, *Advanced Powder Technology* **2021**, *32*, 3845.

[75] a) V. Chanda, D. Blaudszun, L. Hoof, I. Sanjuán, K. Pellumbi, K. junge Puring, C. Andronescu, U.-P. Apfel, *ChemElectroChem* **2024**, *11*; b) A. Loh, X. Li, S. Sluijter, P. Shirvanian, Q. Lai, Y. Liang, *Hydrogen* **2023**, *4*, 257.

Supporting Information

Supporting information is available from the Wiley Online Library or from the authors.

The comparison study of lanthanum-based perovskites reveals that it is essential to combine lab-scale and application-relevant electrochemical analysis. Only in that case it is possible to get a complete picture of how to develop electrocatalysts further. This systematic transition can be achieved by the implementation of a highly structured, coherent workflow that enables a rapid transition and evaluation.

From half-cells to full-cells: across-scale comparative evaluation of lanthanum-based perovskites as high-performance anode materials for the oxygen evolution reaction

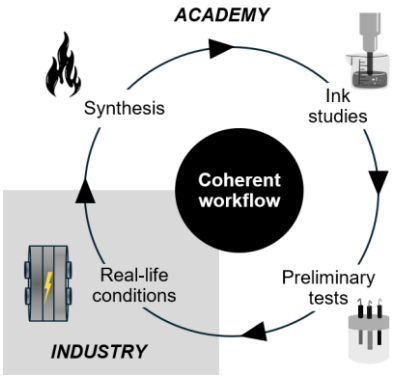

Supporting Information

From half-cells to full-cells: across-scale comparative evaluation of lanthanum-based perovskites as high-performance anode materials for the oxygen evolution reaction

Blaž Toplak[§], Leon Müller[§], Ali Raza Khan, André Olean-Oliveira, Khuzaifa Yahuza Muhammad, Wang Feng, Da Xing, Raíssa Ribeiro Lima Machado, Mohammed-Ali Sheikh, Leander Kucklick, Ahammed Suhail Odungat, Philipp Gerschel, Corina Andronescu, Harry Hoster, Christof Schulz, Viktor Čolić, Ulf-Peter Apfel, Hartmut Wiggers, Mohaned Hammad, and Doris Segets**

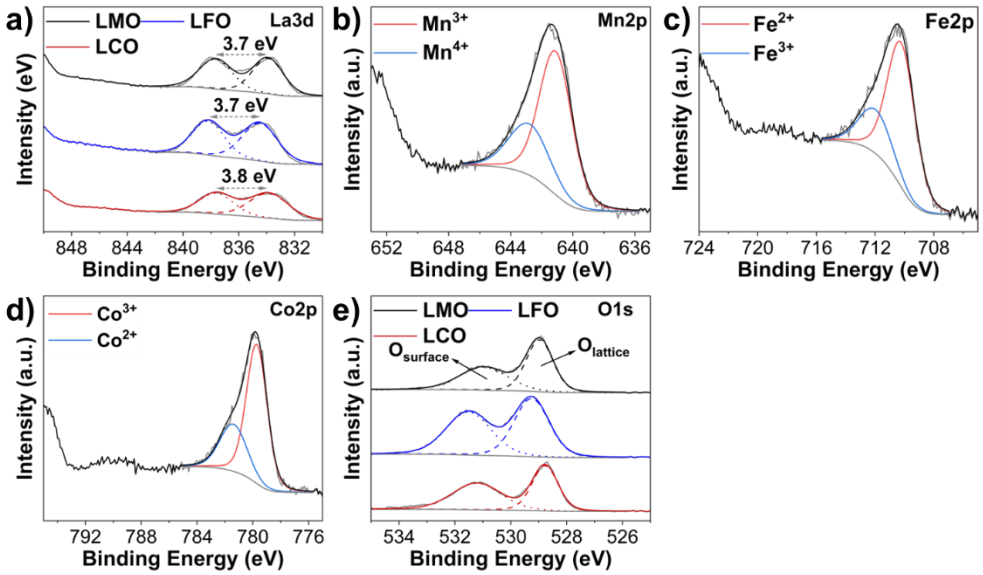

Figure S1. X-ray photoelectron spectra of LMO, LFO, and LCO (a–e) nanoparticles in the La3d$_{5/2}$, Mn2p$_{3/2}$, Fe2p$_{3/2}$, Co2p$_{3/2}$, and O1s region.

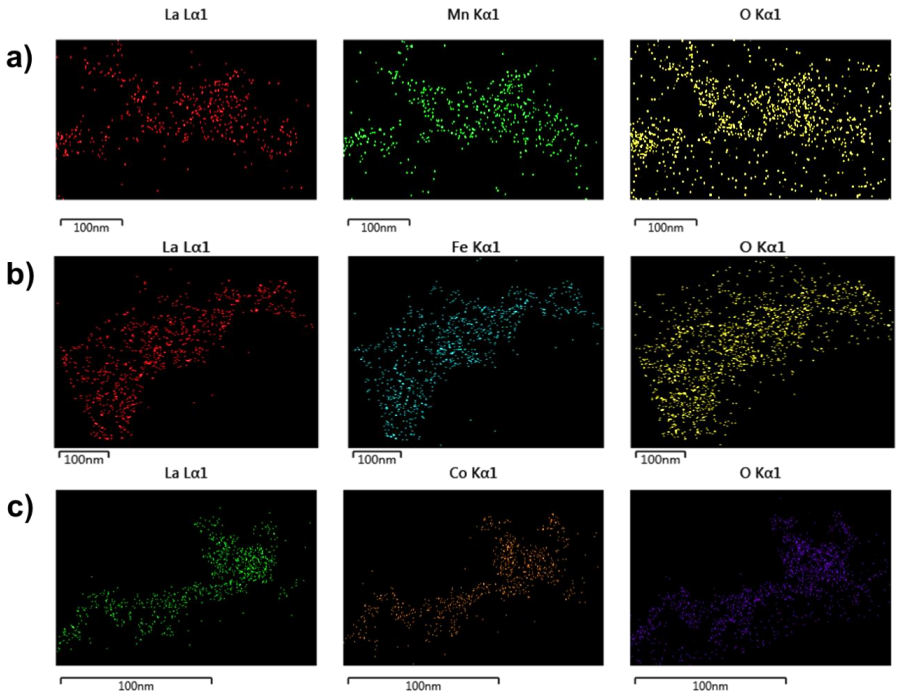

Figure S2. EDX mappings of LMO, LFO, and LCO nanoparticles (a–c) .

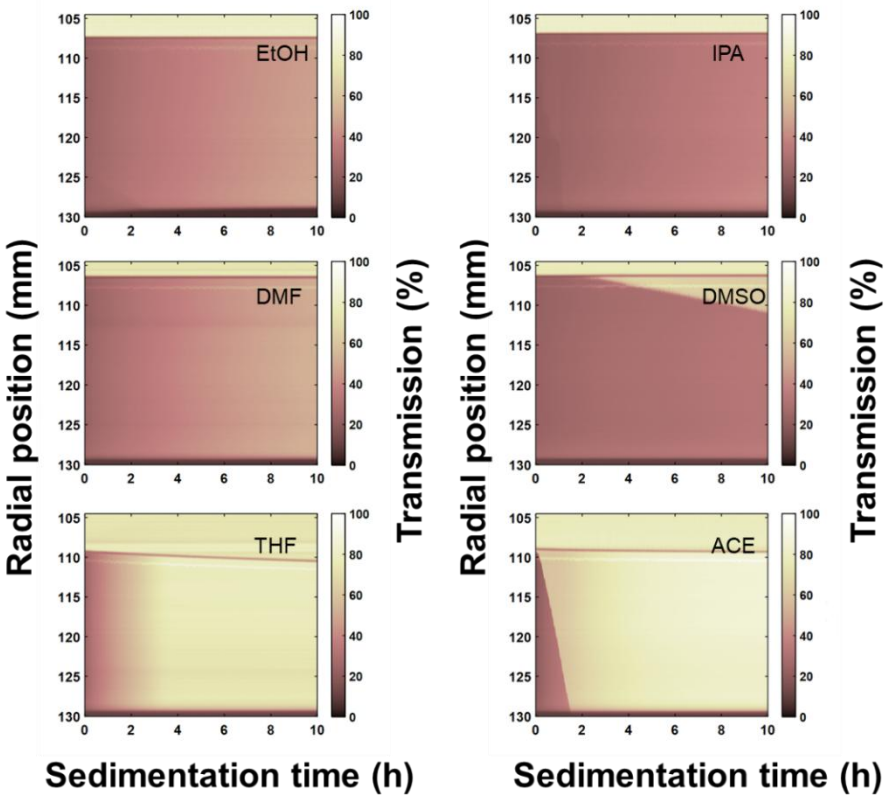

Figure S3. LMO transmittograms in ethanol (EtOH), dimethylformamide (DMF), tetrahydrofuran (THF), 2-propanol (IPA), dimethyl sulfoxide (DMSO, and acetone (ACE).

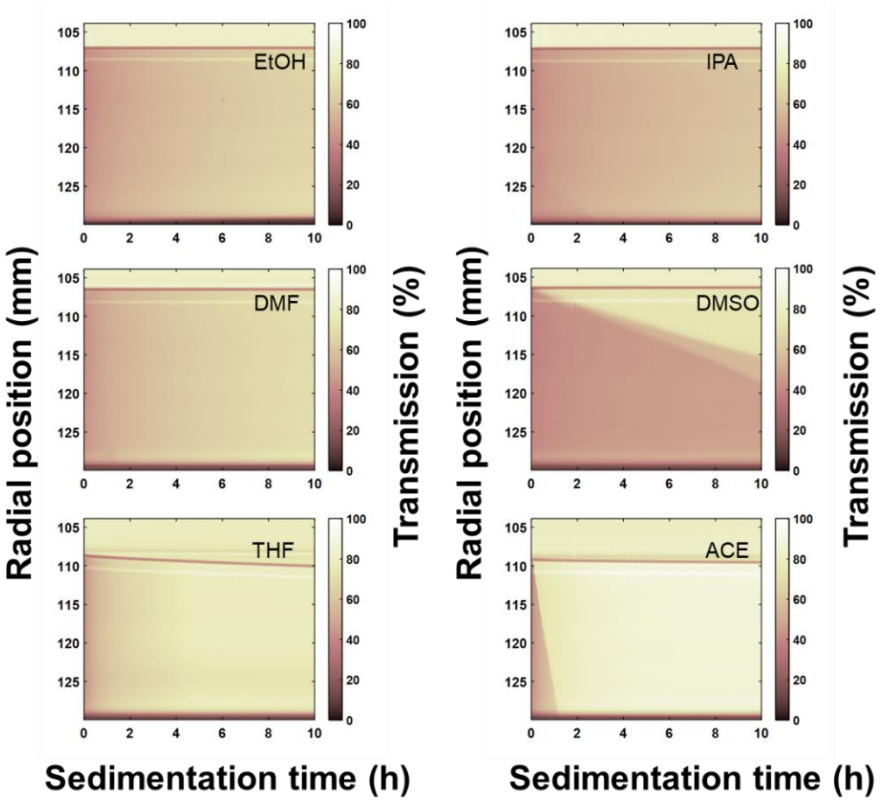

Figure S4. LFO transmittograms in EtOH, DF, THF, IPA, DMSO, and ACE.

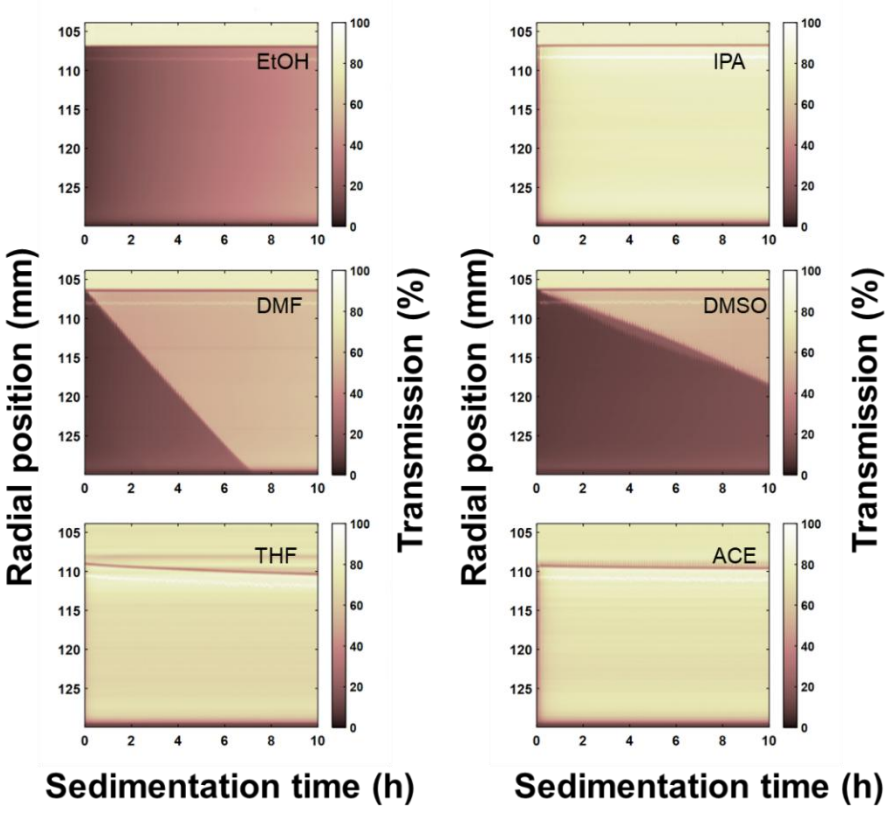

Figure S5. LCO transmittograms in EtOH, DMF, THF, IPA, DMSO, and ACE.

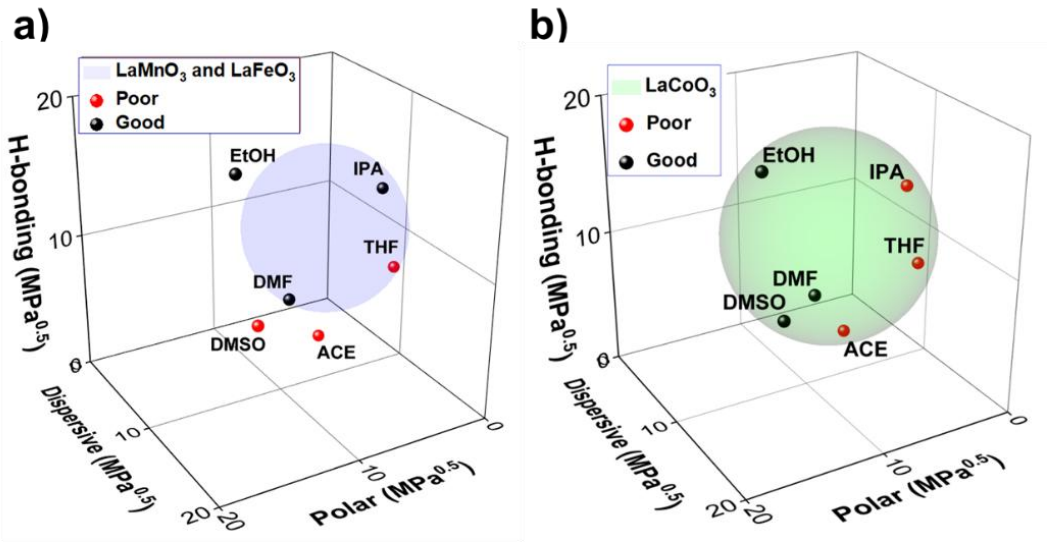

Figure S6. (a) HSP sphere for LMO and LFO nanoparticles, (b) HSP sphere for LCO nanoparticles, calculated with HSPiP 5.4.08 software.

Table S1. HSP parameters of LMO, LFO, and LCO in various probe liquids. δ_D: dispersion interactions, δ_P: polar interactions, δ_H: H-bond interactions, and R: Hansen sphere radius; all values are given in $Mpa^{0.5}$.

	LMO	LFO	LCO
δ_D / $Mpa^{0.5}$	16.5	16.5	17.1
δ_P / $Mpa^{0.5}$	10.7	10.7	12.6
δ_H / $Mpa^{0.5}$	15.0	15.0	14.9
R / $Mpa^{0.5}$	5.1	5.1	6.6

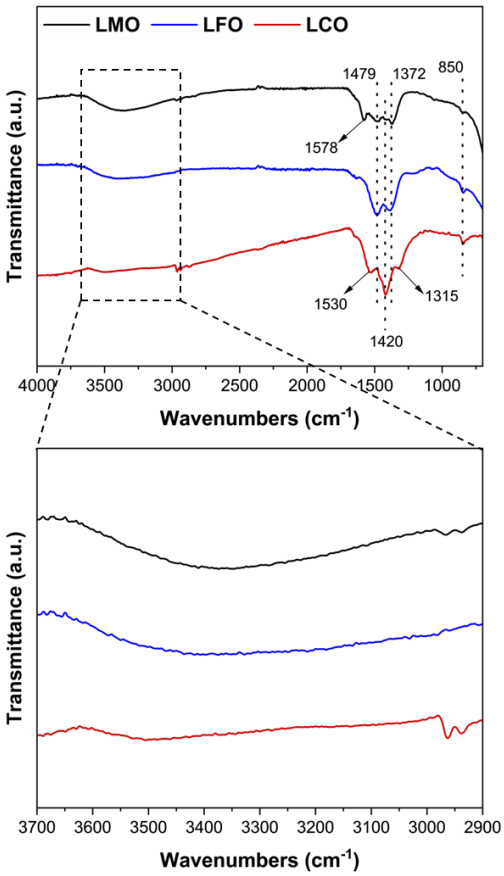

Figure S7. FTIR measurement of LMO, LFO, and LCO, and the enlarged area between 2900 and 3700 cm^{-1}, which is related to the −OH group.

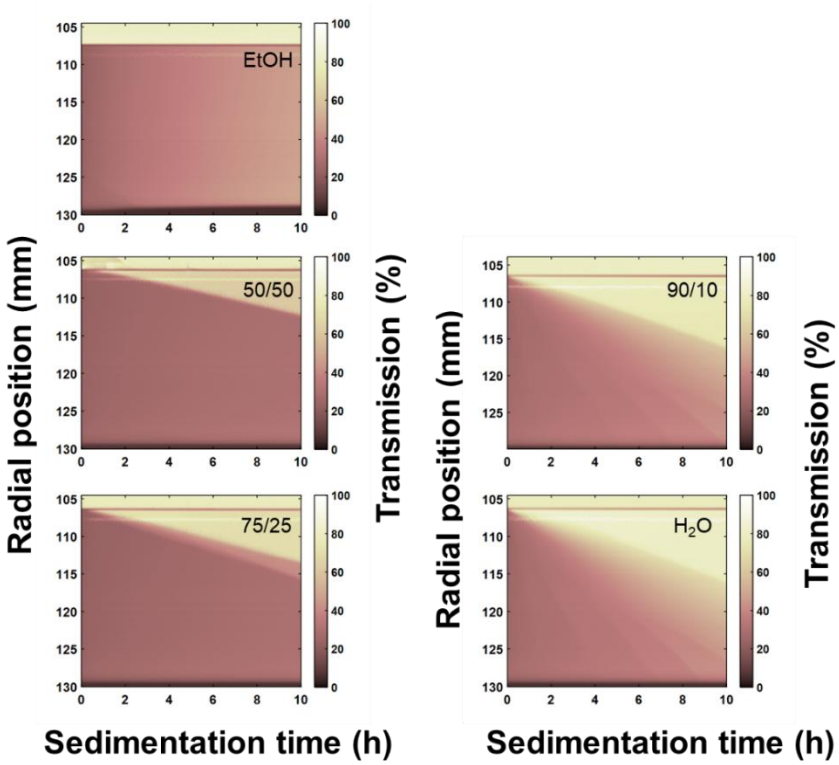

Figure S8. LMO transmittograms in EtOH, MQ H_2O, and various MQ H_2O/EtOH mixtures.

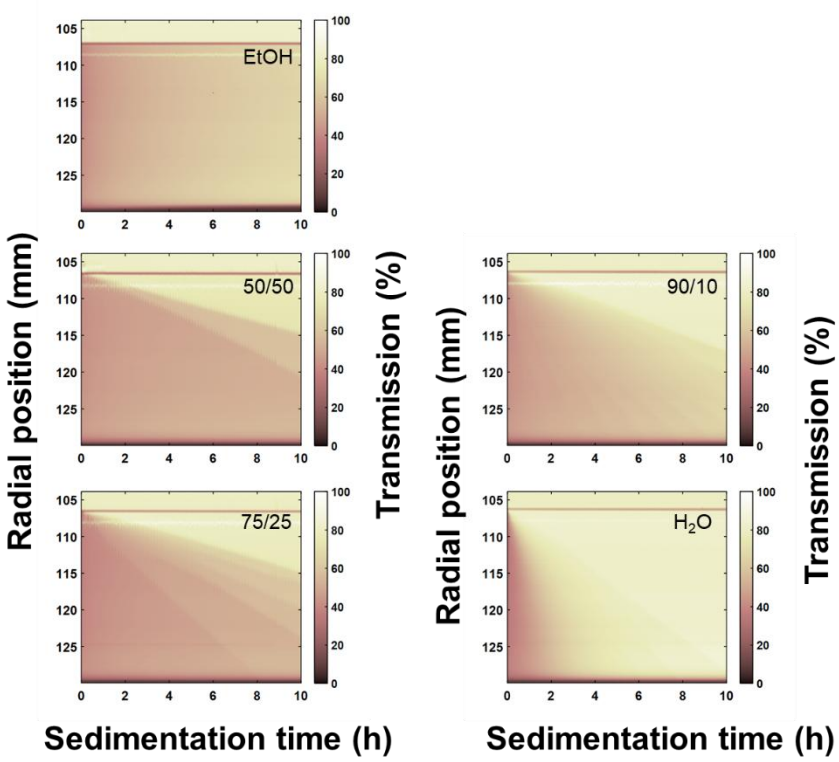

Figure S9. LFO transmittograms in EtOH, MQ H_2O, and various MQ H_2O/EtOH mixtures.

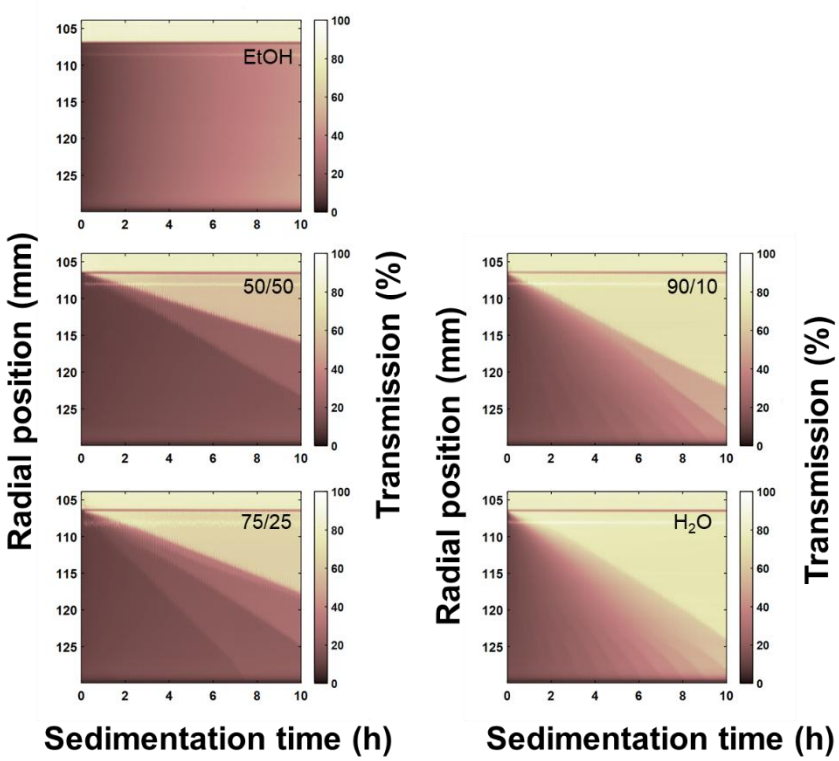

Figure S10. LCO transmittograms in EtOH, MQ H_2O, and various MQ H_2O/EtOH mixtures.

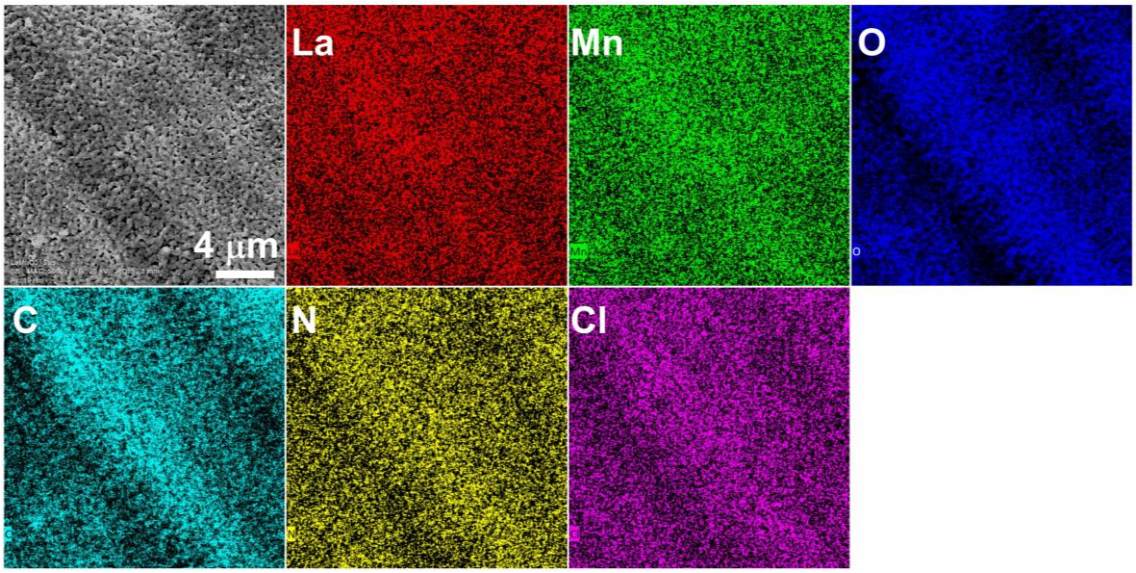

Figure S11. SEM image of LMO-based electrode before electrochemical testing and the corresponding elemental mapping of lanthanum, manganese, oxygen, carbon, nitrogen, and chlorine.

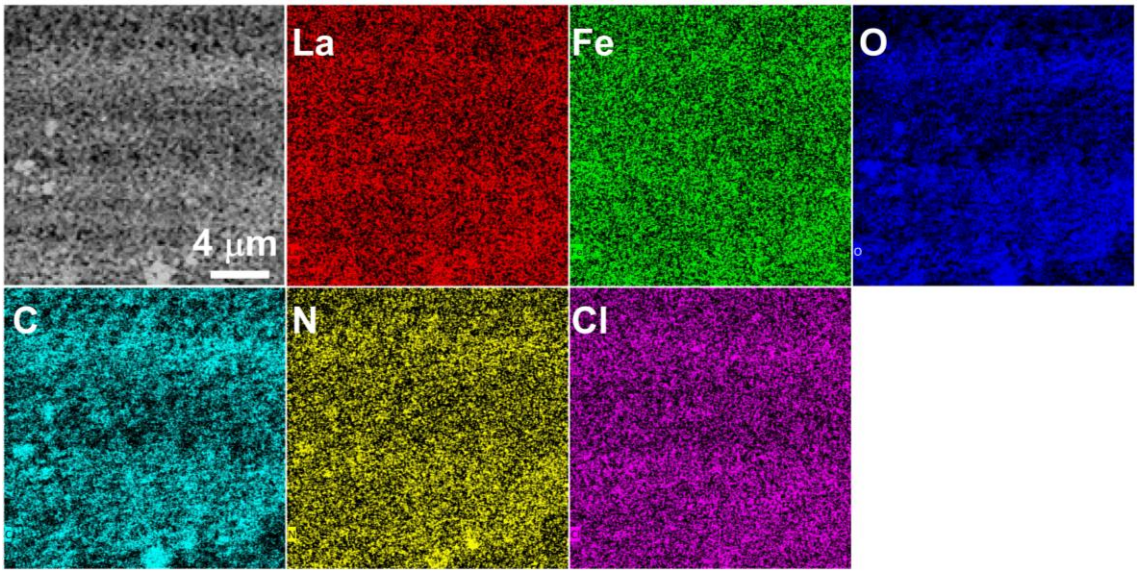

Figure S12. SEM image of LFO-based electrode before electrochemical testing and the corresponding elemental mapping of lanthanum, iron, oxygen, carbon, nitrogen, and chlorine.

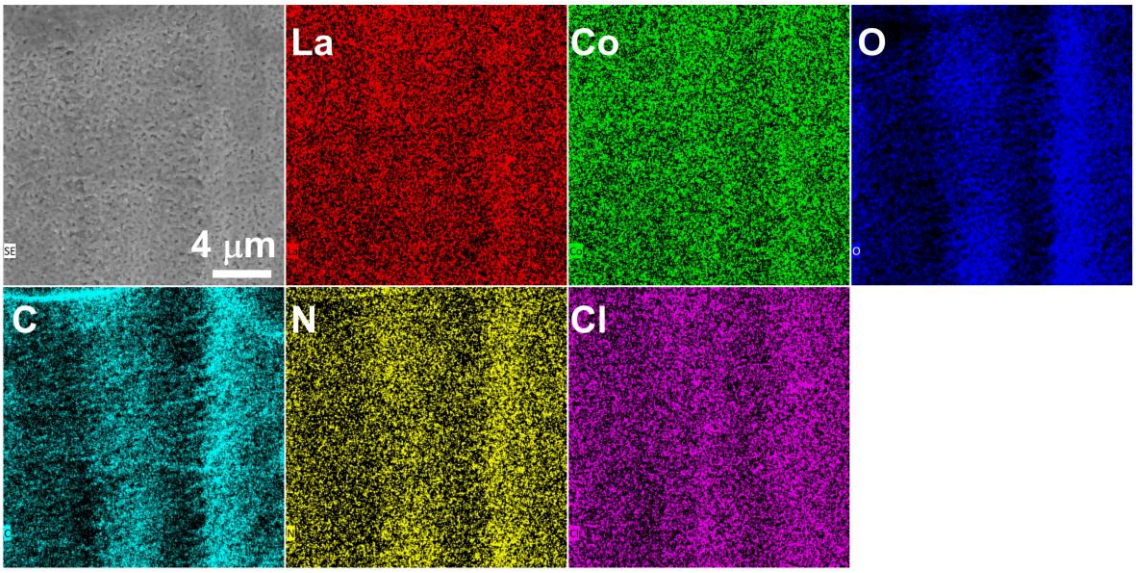

Figure S13. SEM image of LCO-based electrode before electrochemical testing and the corresponding elemental mapping of lanthanum, cobalt, oxygen, carbon, nitrogen, and chlorine.

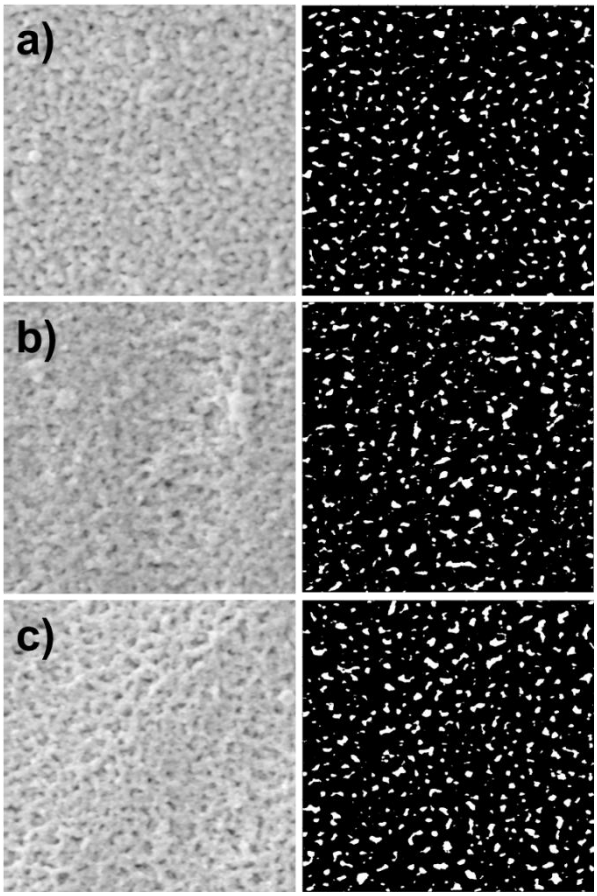

Figure S14. LMO-, LFO-, and LCO-based surface pore coverage (a, b, and c) on the prepared anode substrates.

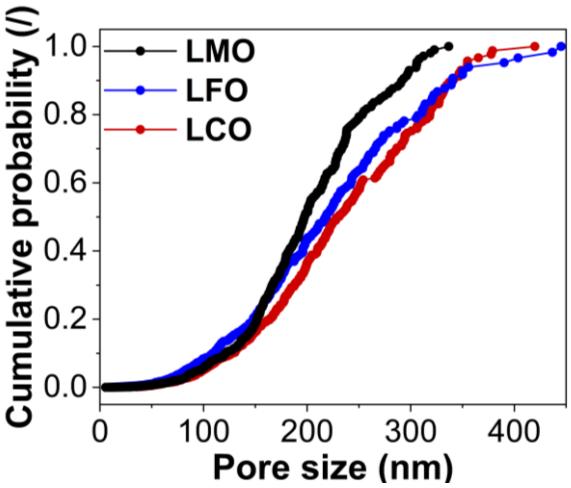

Figure S15. Average pore size distribution on pristine LMO-, LFO-, and LCO-based electrodes (black, blue, and red).

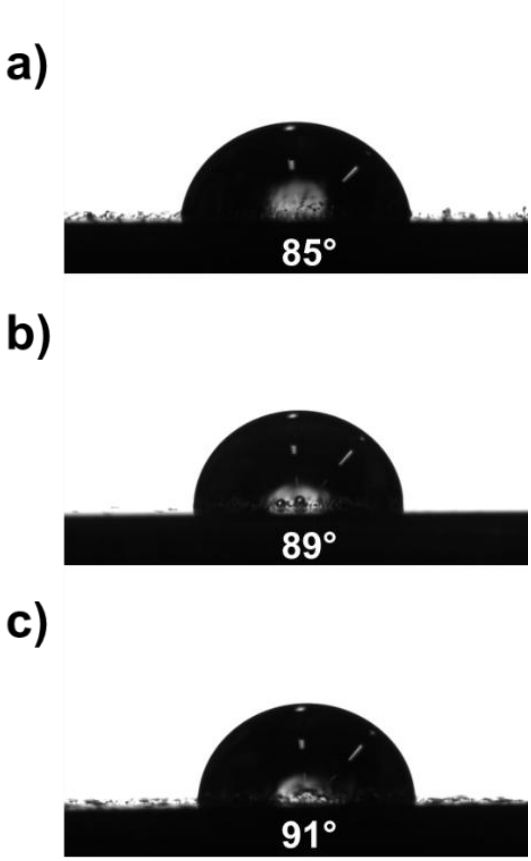

Figure S16. Contact angle measurements with the 1 mol L^{-1} purified KOH on LMO- (a), LFO- (b), and LCO-based electrodes (c).

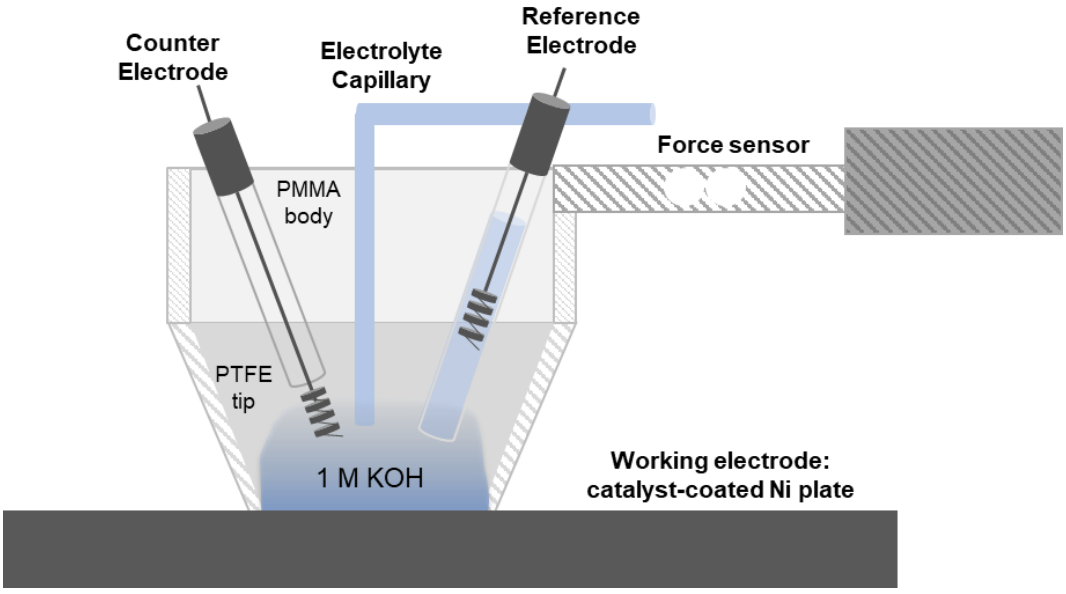

Figure S17. Schematic representation of a scanning droplet cell setup.

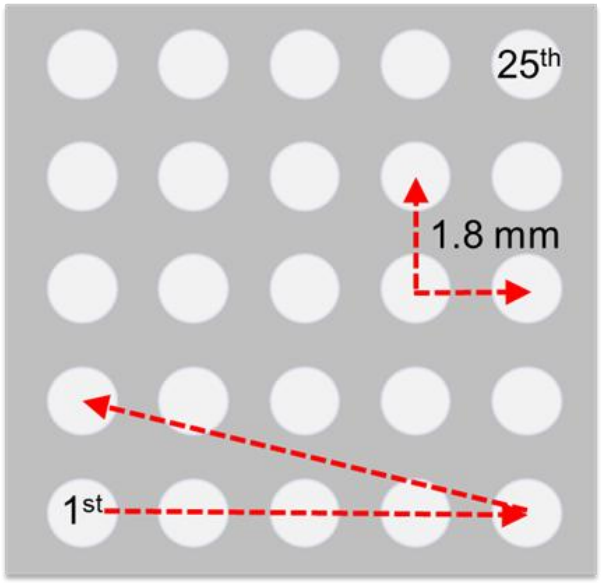

Figure S18. Visualization of scanning droplet cell grid pattern measurement procedure.

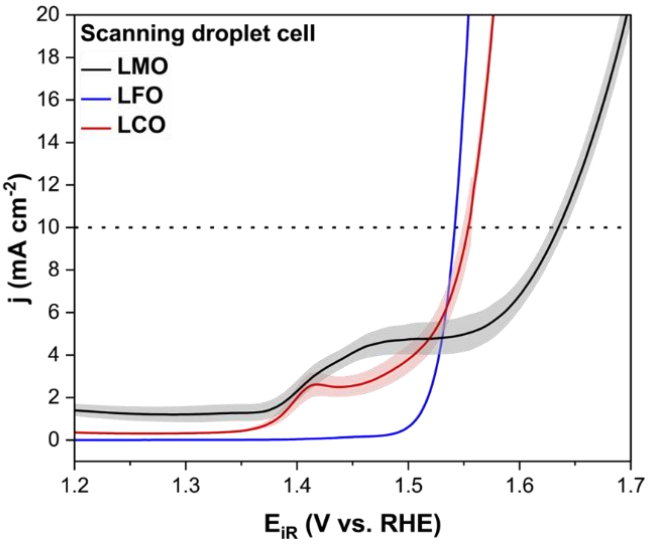

Figure S19. Average LSVs of the individual spots of each 1×1 cm^2 nickel plate coated with LMO- (black), LFO- (blue), or LCO-based electrodes (red) with Sustainion®. LSVs were recorded with SDC in O_2-saturated, purified 1M KOH at a 5 mV s^{-1} scan rate. The solid lines correspond to the mean values, and the shadows represent their standard deviations.

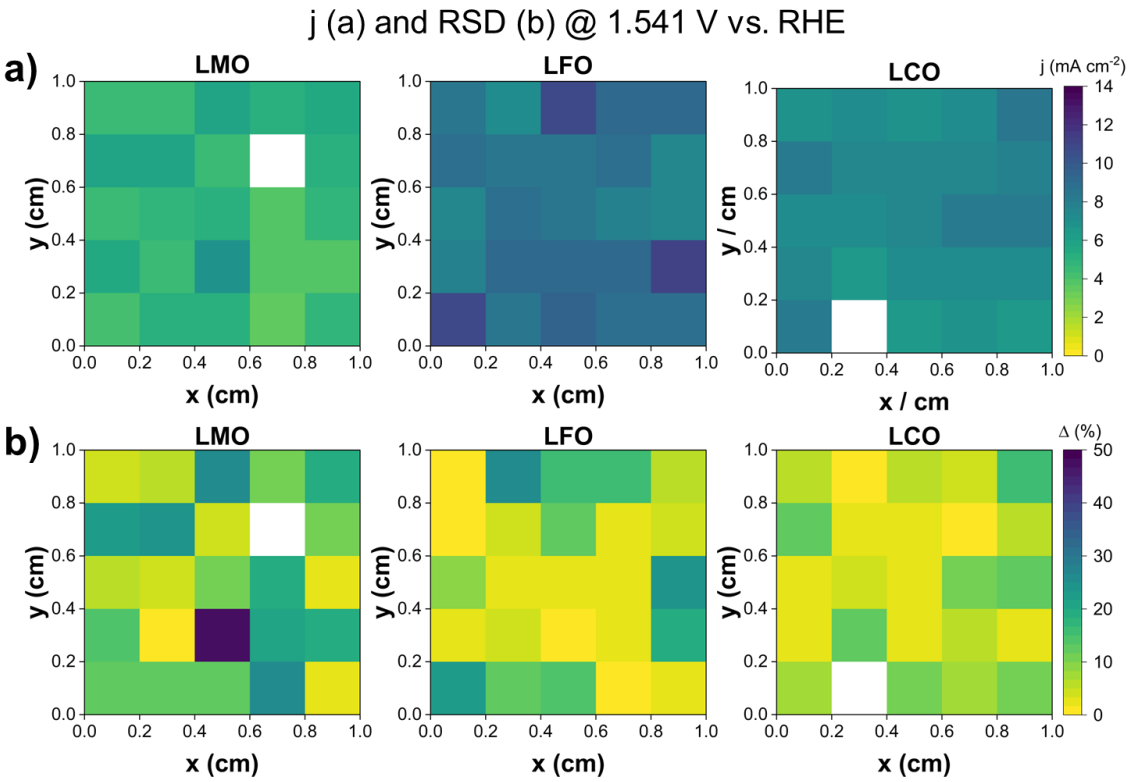

Figure S20. Activity map of the current densities of the LMO, LFO, and LCO coated nickel plates with Sustainion as a binder obtained with SDC (a) and their standard deviations(b). Invalid measurements are displayed in white color.

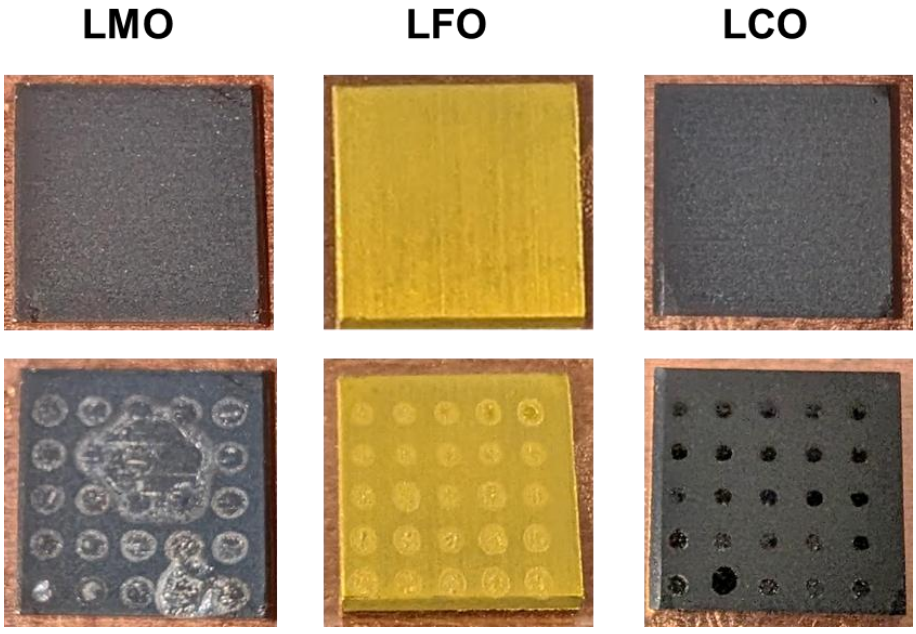

Figure S21. LMO- (left), LFO- (middle), and LCO-based (right) electrodes before (up) and after (down) electrochemical testing with the SDC setup on 25 spots.

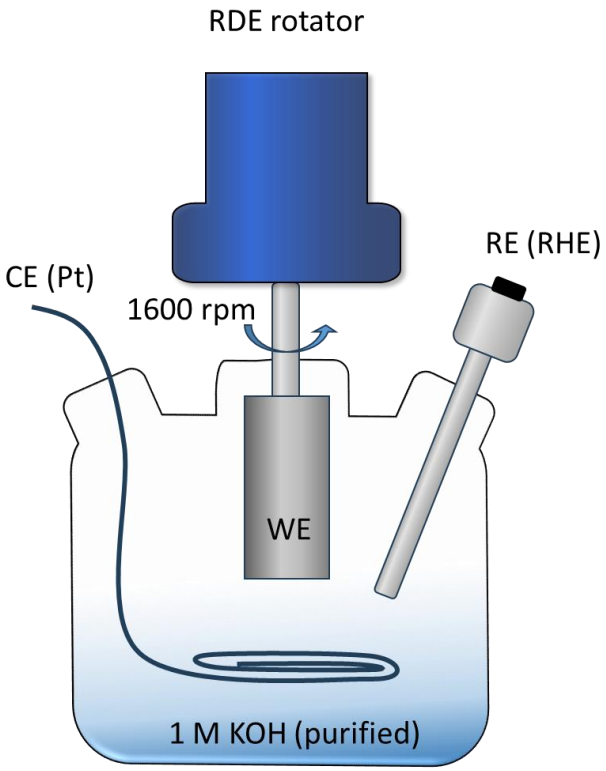

Figure S22. Schematic representation of rotational disc electrode setup. WE – working electrode, CE – Pt counter electrode, and RE – reference electrode.

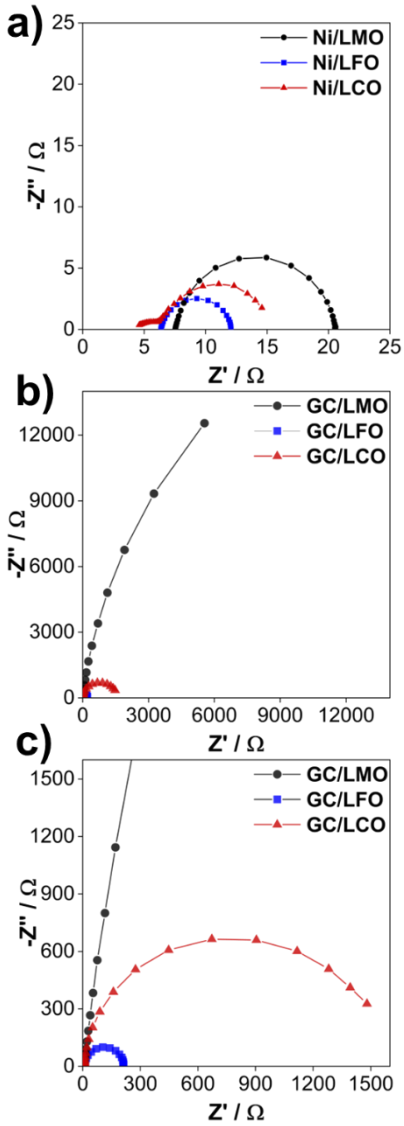

Figure S23. Nyquist plots of LMO-, LFO-, and LCO-based electrodes (black, blue, and red) on nickel (a) and glassy-carbon substrate (b, c). (c) Presents a magnification of figure (b).

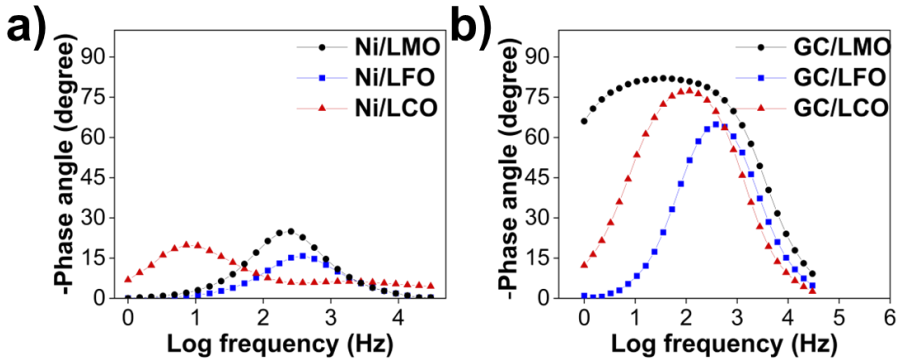

Figure S24. Bode plots of LMO-, LFO-, and LCO-based electrodes (black, blue, and red) on nickel and glassy-carbon substrate (a, b).

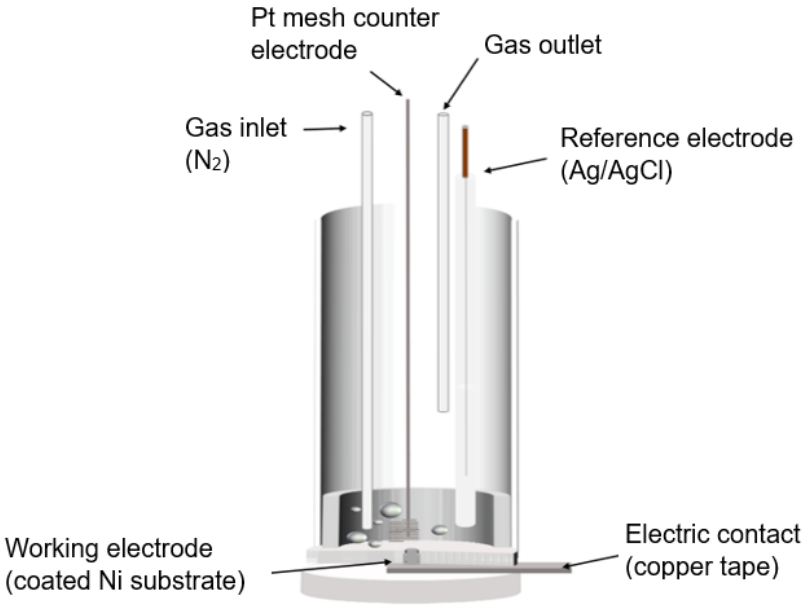

Figure S25. Schematic representation of a compression cell. Reproduced under terms of the CC-BY license.[13] 2024, Gerschel et al., published by Wiley Online Library.

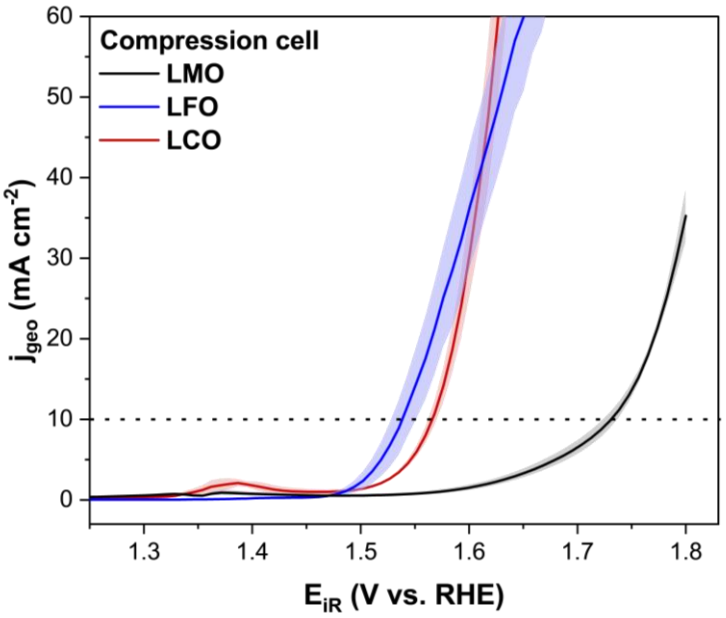

Figure S26. LSV of LMO- (black), LFO- (blue), and LCO-based electrodes (red) with Sustainion® recorded with the compression cell in O_2-saturated, purified 1 mol L^{-1} KOH at a 5 mV s^{-1} scan rate. The solid lines correspond to the mean values, and the shadows represent their standard deviations.

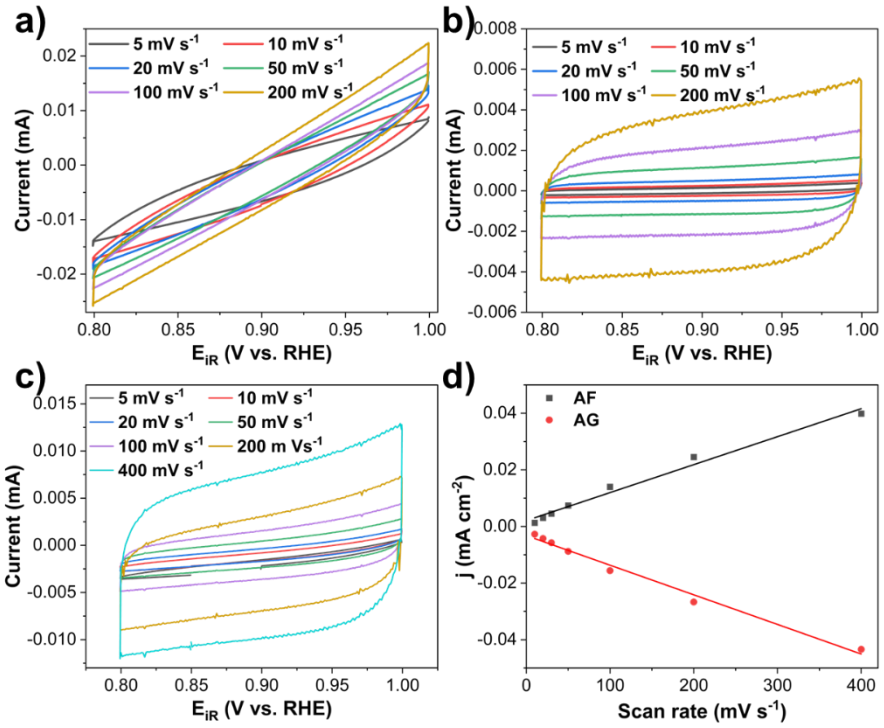

Figure S27. CVs for the determination of C_{dl} in purified 1 mol L^{-1} KOH solution for LMO-, LFO-, and LCO-based electrodes (a–c). Linear (AF - black and AL – red) fitting of the recorded double-layer charging currents (d).

Table S2. AF and AG linear regression parameters are used to determine the ECSA of LMO-, LFO-, and LCO-based electrodes.

■AF	
Slope	9.87765E-5 ± 5.64706E-6
Pearson's r	0.99193
R-Square (COD)	0.98392
Adj. R-Square	0.9807
●AG	
Slope	-1.04598E-4 ± 5.3022E-6
Pearson's r	-0.99364
R-Square (COD)	0.98731
Adj. R-Square	0.98478

Table S3. Electrochemical active surface area (ECSA) data of the perovskite electrocatalytic materials in the compression cell. The C_{dl} was determined using an electrochemical technique (CV). ECSAs were calculated using the formula ECSA = C_{dl}/C_s, with C_s = 40 µF.

	LMO	LFO	LCO
Slope	12.26	18.75	22.07
$\boldsymbol{C}_{dl}$ / µF	62.55	95.66	112.55
$\boldsymbol{R}_f$	1.55	2.39	2.81
ECSA / cm^{-2}	0.30	0.57	0.55

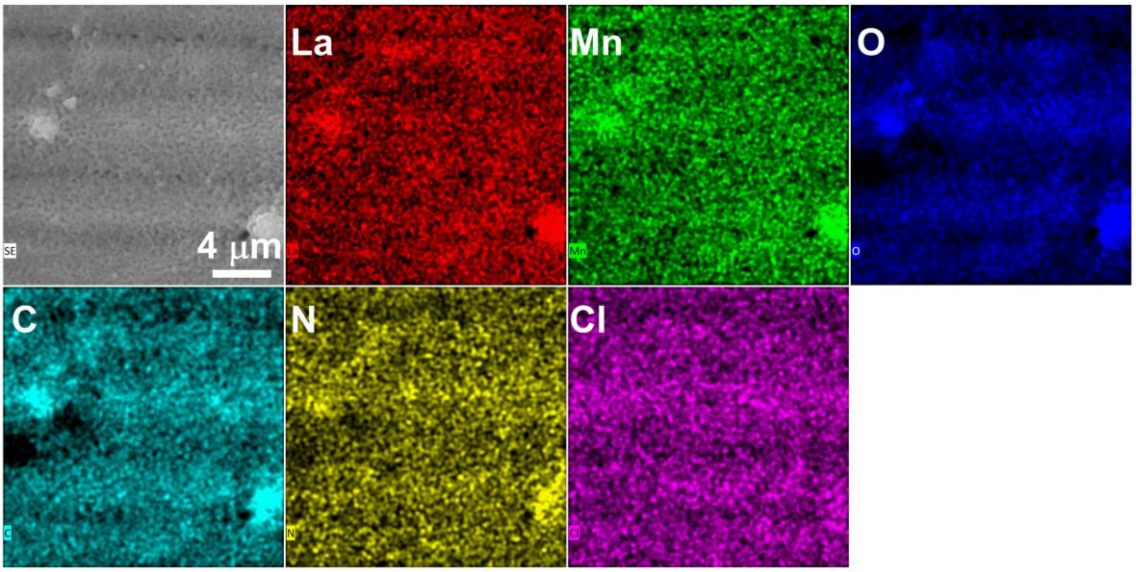

Figure S28. SEM image of LMO-based electrode after electrochemical testing and the corresponding elemental mapping of lanthanum, manganese, oxygen, carbon, nitrogen, and chlorine.

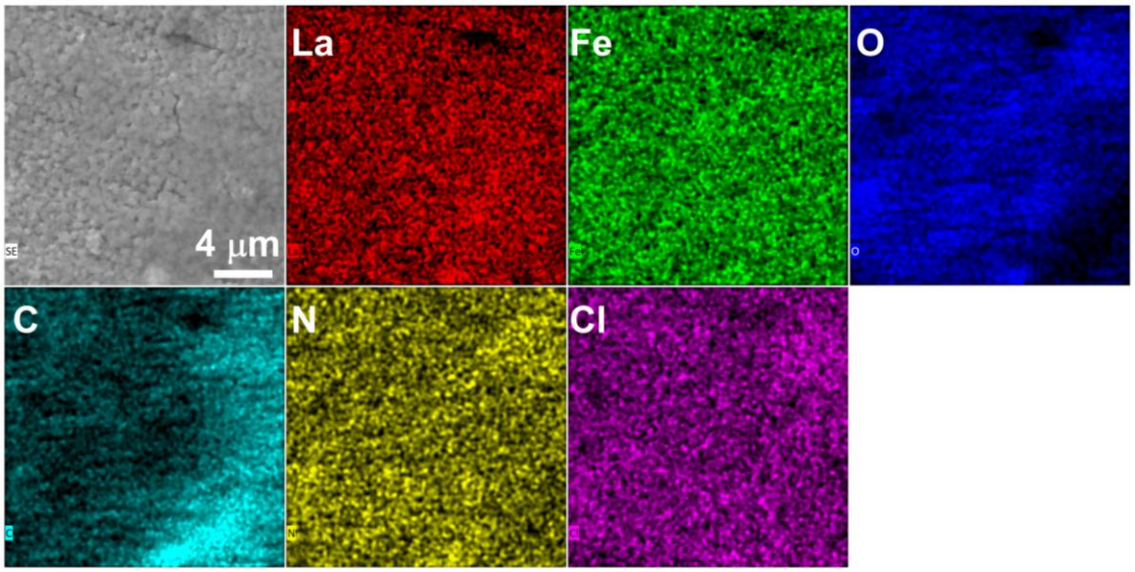

Figure S29 SEM image of LFO-based electrode after electrochemical testing and corresponding elemental mapping of lanthanum, iron, oxygen, carbon, nitrogen, and chlorine.

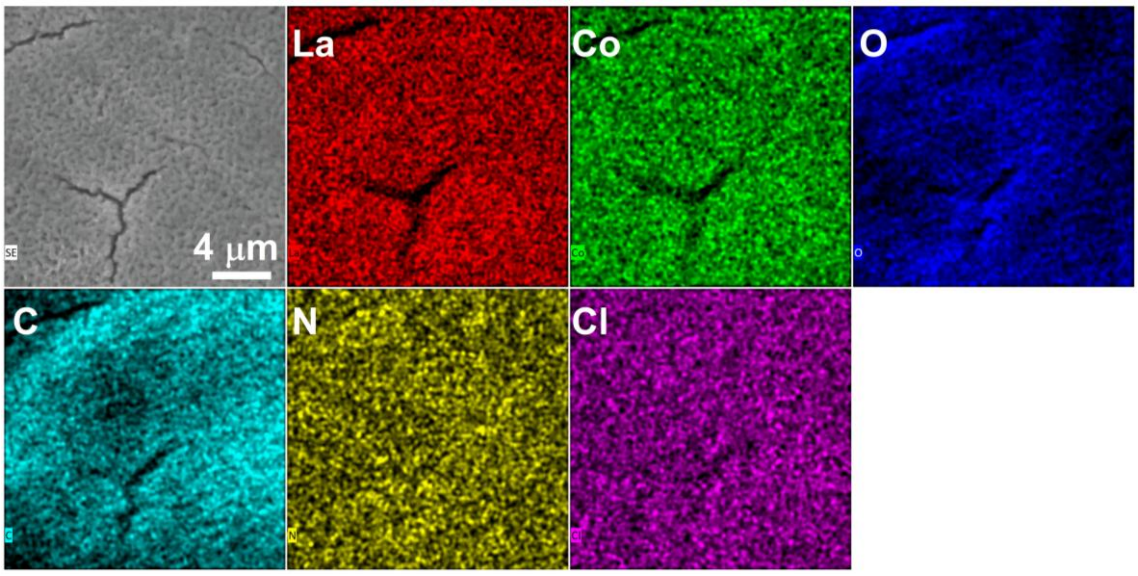

Figure S30. SEM image of LCO-based electrode after electrochemical testing and corresponding elemental mapping of lanthanum, cobalt, oxygen, carbon, nitrogen, and chlorine.

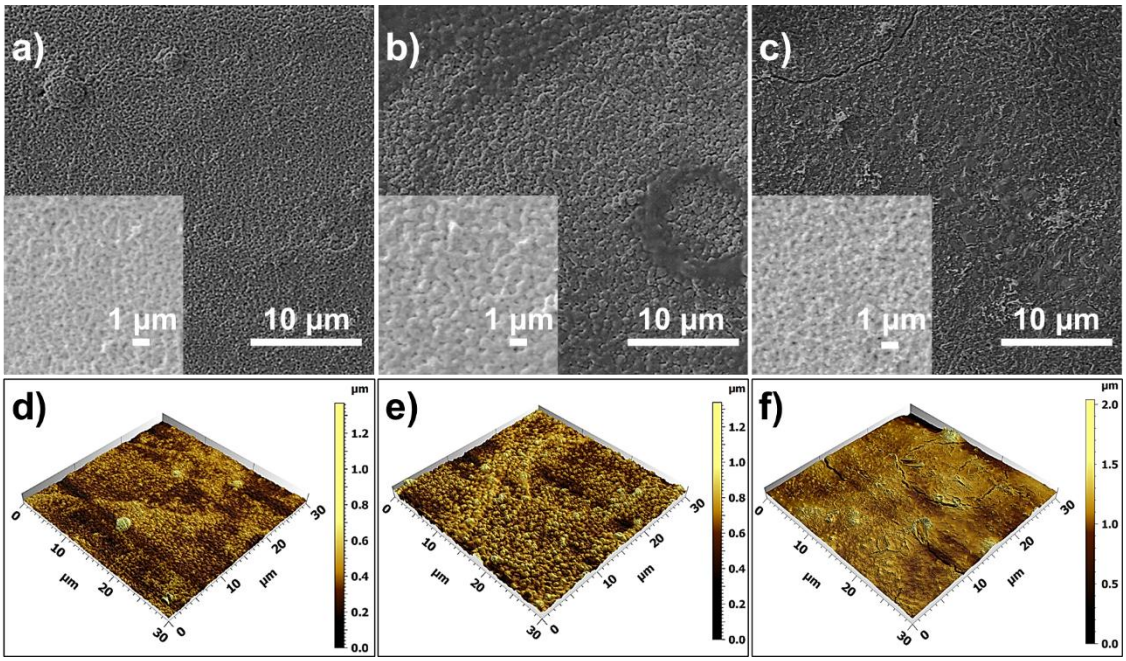

Figure S31. SEM (a–c) and AFM (d-f) images of LMO-, LFO-, and LCO-based electrodes after electrochemical testing in a compression cell for 12 h. AFM measurements are taken on a 30×30 µm^2 area.

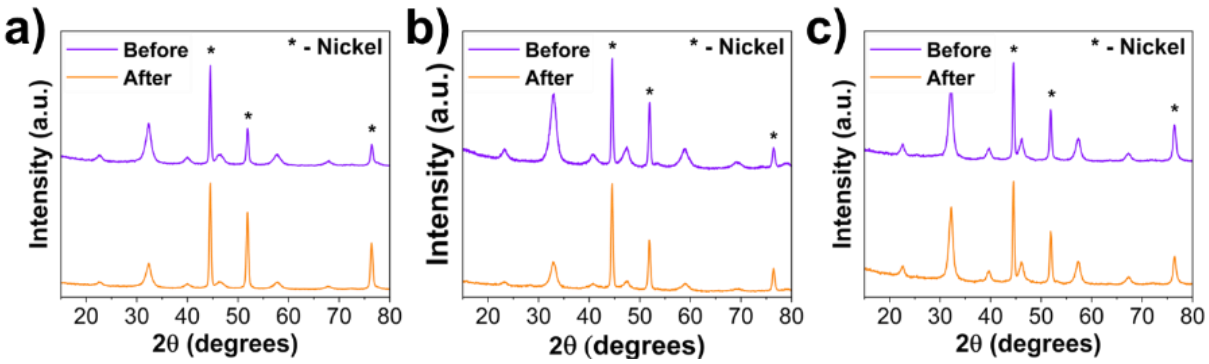

Figure S32. X-ray diffraction pattern of LMO- (a), LFO- (b), and LCO-based electrodes (c) in GIXRD mode before and after electrochemical testing (magenta, orange) in a compression cell. The star represents the signal from the nickel substrate.

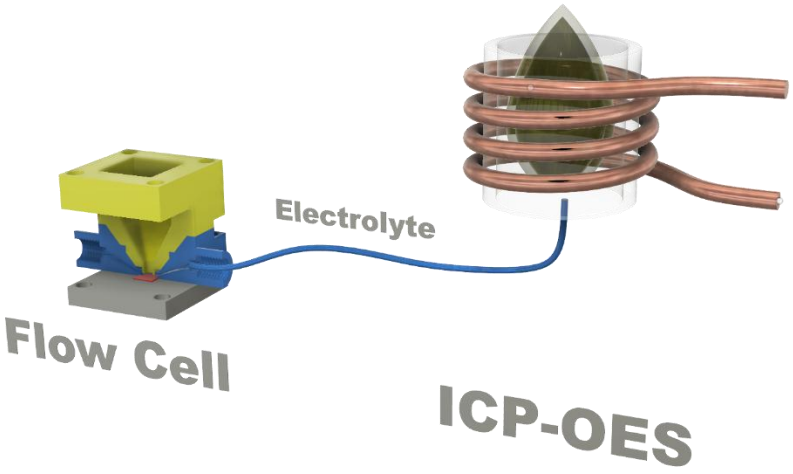

Figure S33. Schematic representation of a flow cell coupled with the ICP-OES.

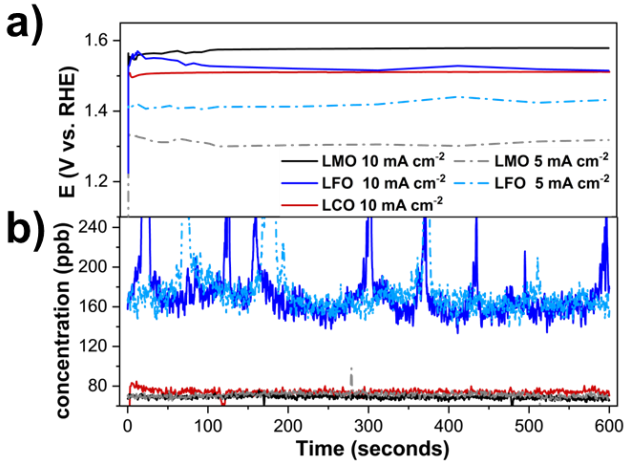

Figure S34. CP measurements performed with the flow cell (a) coupled with ICP-OES (b) at 5 and 10 mA cm^{-2} (light and dark) in O_2-saturated, purified 1 mol L^{-1} KOH.

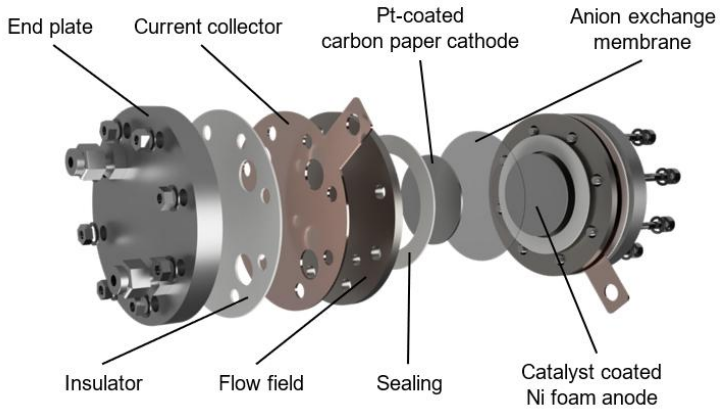

Figure S35. Schematic representation of zero-gap full-cell. Reproduced under terms of the CC-BY license.[1] Copyright 2024, Gerschel et al., published by Wiley Online Library.

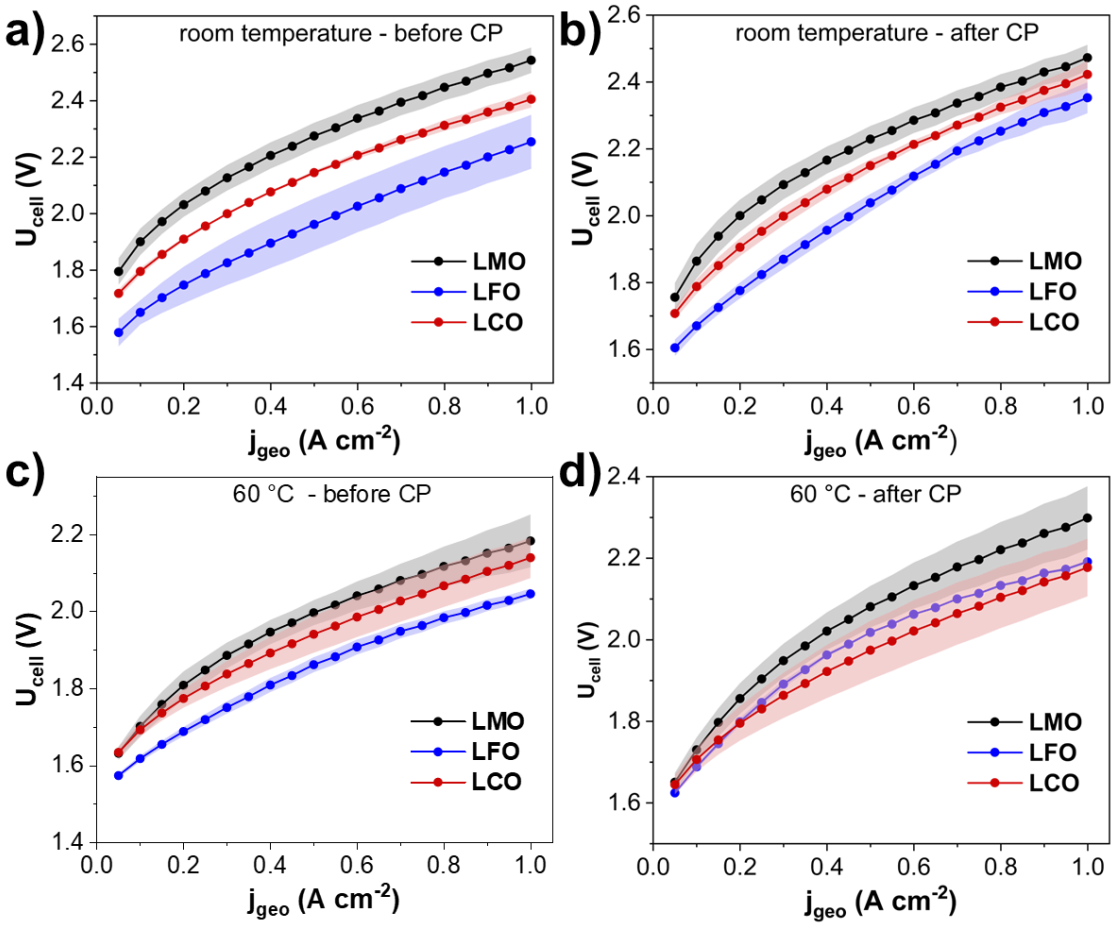

Figure S36. Polarization curves obtained with the zero-gap full-cell before and after stability testing for 12 h at room temperature (a, b), and before and after stability measurements for 24 h at 60 °C (c, d) in 1 mol L^{-1} KOH. The solid lines of LMO-, LFO-, and LCO-based electrodes (black, blue, red) correspond to the mean values, and the shadows represent their standard deviations.

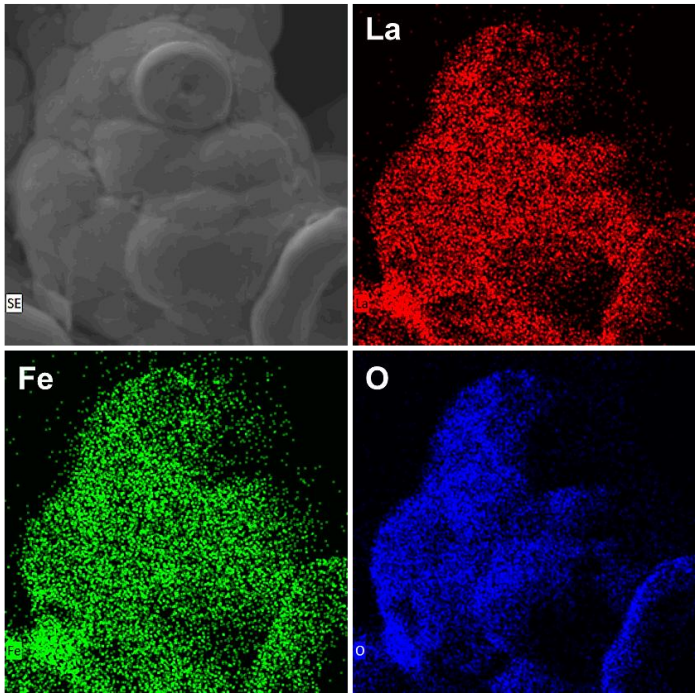

Figure S37. (a) SEM image of LFO-based electrode after electrochemical testing at 60 °C in a zero-gap full-cell at 0.5 A cm^{-2} and the corresponding elemental mapping of lanthanum, iron, and oxygen.

Table S4. Atomic ratios of La, Fe, and O on the electrode after electrochemical testing at 60 °C.

Element	La	Fe	O
Atomic ratio / at%	5.7	8.2	86.1

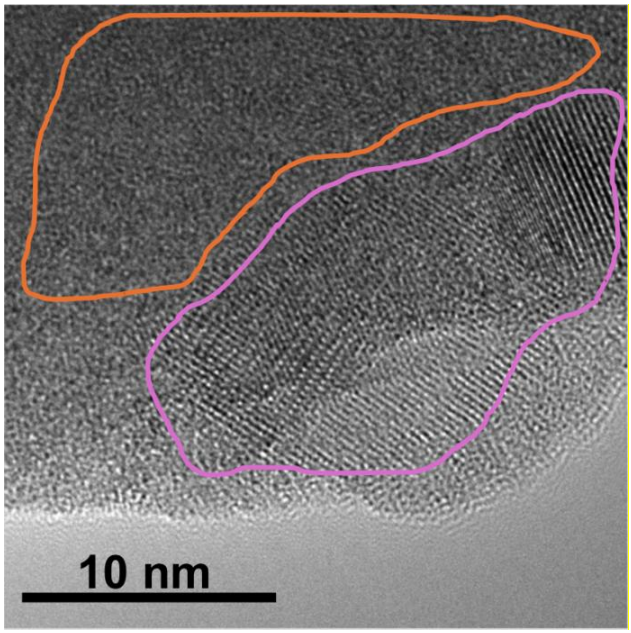

Figure S38. TEM image of LCO-based electrode after the electrochemical testing at 60 °C in a zero-gap full-cell at 0.5 A cm^{-2}. The orange area shows the presence of an amorphous phase, and the pink area shows a crystalline structure.

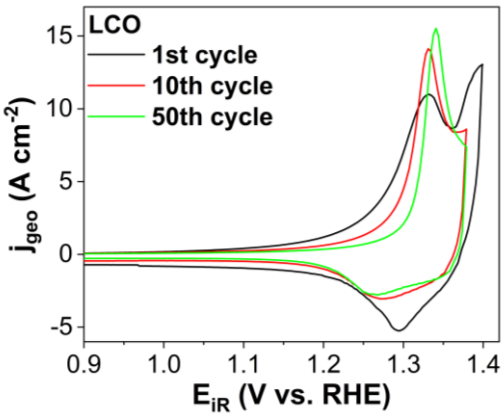

Figure S39. CV cycles of the LCO-based electrode obtained with the compression cell.

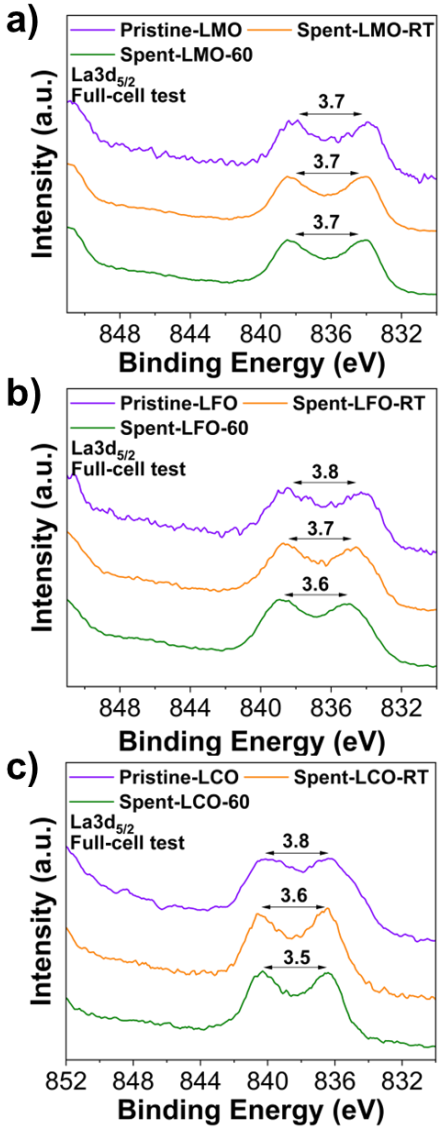

Figure 40. La3d$_{5/2}$ spectra of LMO, LFO, and LCO (a, b, and c), measured on Pristine electrodes and electrodes after electrochemical testing at room temperature and 60 °C (Spent-RT and Spent-60) in zero-gap full-cell (magenta, orange, and green).

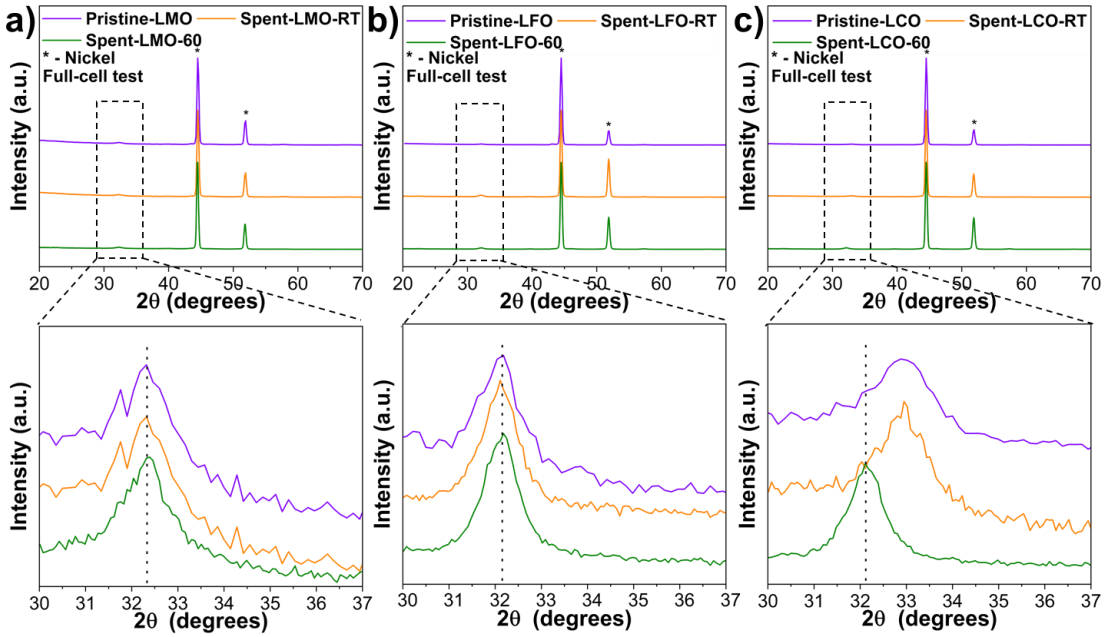

Figure S41. X-ray diffraction in GIXRD mode of (a) LMO-, (b) LFO-, and (c) LCO-based electrode on pristine (purple), tested at 0.5 A cm^{-2} in as-prepared 1 mol L^{-1} KOH for 12 h in a zero-gap full-cell at room temperature (spent-RT, orange), and electrode tested for 24 h in a zero-gap full-cell at 60 °C (spent-60, green). The star represents the nickel foam substrate. Under the full measurement area is an enlarged peak related to the perovskite.

The energy input was determined following the standardized procedure of NANoREG D4.12 SOP. Temperature measurements were obtained while a known mass of water was heated using a Branson 550 sonifier with 3 mm sonication. Styrofoam cushioning was used to prevent heating losses. For the calculations, it was assumed that there were no losses to the surrounding environment, and all acoustic energy was transferred to the water. The acoustic power (P) can be calculated according to the Equation (S1).

$$P = c_p m \frac{\Delta T}{\Delta t} \quad \text{S1}$$

Where c_p is the specific heat capacity of the liquid ($c_{p,\text{water}}$ = 4.18 J kg^{-1} K^{-1}), m is the mass of the liquid, and $\Delta T/\Delta t$ is the slope of the regression curve. The heating characteristics were measured at 20 and 40 %. The resulting heating curves are plotted below in Figure S38.

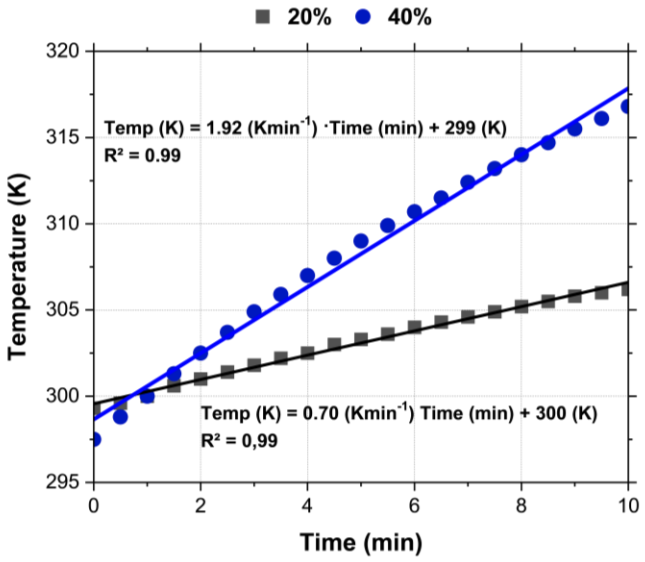

Figure S42: Heating curves at 20 and 40 % amplitude of the Branson 550 sonifier with 3 mm sonication tip. Reproduced under terms of the CC-BY license.[2] Copyright 2023, Anwar et al., published by Wiley Online Library.

References

[1] P. Gerschel, S. Angel, M. Hammad, A. Olean-Oliveira, B. Toplak, V. Chanda, R. Martínez-Hincapié, S. Sanden, A. R. Khan, Da Xing et al., *Carbon Energy* **2024**.

[2] O. Anwar, A. S. Amin, A. Amin, M.-A. Kräenbring, F. Özcan, D. Segets, *Part & Part Syst Charact* **2023**, *40*.